NAVAL POSTGRADUATE SCHOOL

MONTEREY, CALIFORNIA

THESIS

OPTICAL JITTER EFFECTS ON TARGET DETECTION AND TRACKING OF OVERHEAD PERSISTENT INFRARED SYSTEMS

by

Christopher R. Flores

December 2015

Thesis Advisor: Jae Jun Kim
Co-Advisor: Brij N. Agrawal

Approved for public release; distribution is unlimited

THIS PAGE INTENTIONALLY LEFT BLANK

REPORT DOCUMENTATION PAGE			*Form Approved OMB No. 0704–0188*
Public reporting burden for this collection of information is estimated to average 1 hour per response, including the time for reviewing instruction, searching existing data sources, gathering and maintaining the data needed, and completing and reviewing the collection of information. Send comments regarding this burden estimate or any other aspect of this collection of information, including suggestions for reducing this burden, to Washington headquarters Services, Directorate for Information Operations and Reports, 1215 Jefferson Davis Highway, Suite 1204, Arlington, VA 22202-4302, and to the Office of Management and Budget, Paperwork Reduction Project (0704-0188) Washington, DC 20503.			
1. AGENCY USE ONLY ***(Leave blank)***	**2. REPORT DATE** December 2015	**3. REPORT TYPE AND DATES COVERED** Master's thesis	
4. TITLE AND SUBTITLE OPTICAL JITTER EFFECTS ON TARGET DETECTION AND TRACKING OF OVERHEAD PERSISTENT INFRARED SYSTEMS			**5. FUNDING NUMBERS**
6. AUTHOR(S) Christopher R. Flores			
7. PERFORMING ORGANIZATION NAME(S) AND ADDRESS(ES) Naval Postgraduate School Monterey, CA 93943-5000			**8. PERFORMING ORGANIZATION REPORT NUMBER**
9. SPONSORING /MONITORING AGENCY NAME(S) AND ADDRESS(ES) N/A			**10. SPONSORING / MONITORING AGENCY REPORT NUMBER**
11. SUPPLEMENTARY NOTES The views expressed in this thesis are those of the author and do not reflect the official policy or position of the Department of Defense or the U.S. Government. IRB Protocol number ____N/A____.			
12a. DISTRIBUTION / AVAILABILITY STATEMENT Approved for public release; distribution is unlimited			**12b. DISTRIBUTION CODE**

13. ABSTRACT (maximum 200 words)

The purpose of this thesis is to provide a system level performance analysis for an imaging spacecraft. In an imaging spacecraft, an attitude control subsystem's function is to orient the spacecraft's body to acquire a target through the use of an actuator. In practice, reaction wheels commonly perform this function by producing a reactive torque on the spacecraft. Consequently, due to the static and dynamic imbalances in individual reaction wheels, an undesired vibration, called jitter, is generated during operation and causes variations in the spacecraft's attitude. Focusing on missions and payloads operating in the infrared band, optical jitter effects on target detection and tracking performance need to be investigated.

Using a quaternion error feedback design, jitter produced by the reaction wheels was recorded while performing a standard spacecraft maneuver. Simulating a low earth orbiting satellite, the vibrations generated a significant optical jitter blur due to a line-of-sight motion. After implementing the optical jitter blur in a baseline high resolution image, the simulation considerably reduced the frame's spatial resolution and intensity. The simulation demonstrated the jitter blur's effects on spatial resolution and intensity, which significantly decreased the system's ability to detect and track objects-of-interest.

14. SUBJECT TERMS infrared detection and tracking, centroid, jitter, reaction wheel, blur, Kalman filter			**15. NUMBER OF PAGES** 79
			16. PRICE CODE
17. SECURITY CLASSIFICATION OF REPORT Unclassified	**18. SECURITY CLASSIFICATION OF THIS PAGE** Unclassified	**19. SECURITY CLASSIFICATION OF ABSTRACT** Unclassified	**20. LIMITATION OF ABSTRACT** UU

NSN 7540–01-280-5500 Standard Form 298 (Rev. 2–89)
Prescribed by ANSI Std. 239–18

THIS PAGE INTENTIONALLY LEFT BLANK

Approved for public release; distribution is unlimited

OPTICAL JITTER EFFECTS ON TARGET DETECTION AND TRACKING OF OVERHEAD PERSISTENT INFRARED SYSTEMS

Christopher R. Flores
Lieutenant, United States Navy
B.S., United States Naval Academy, 2007

Submitted in partial fulfillment of the
requirements for the degree of

MASTER OF SCIENCE IN ASTRONAUTICAL ENGINEERING

from the

NAVAL POSTGRADUATE SCHOOL
December 2015

Approved by: Jae Jun Kim
Thesis Advisor

Brij N. Agrawal
Thesis Co-Advisor

Garth V. Hobson
Chair, Department of Mechanical and Aerospace Engineering

THIS PAGE INTENTIONALLY LEFT BLANK

ABSTRACT

The purpose of this thesis is to provide a system level performance analysis for an imaging spacecraft. In an imaging spacecraft, an attitude control subsystem's function is to orient the spacecraft's body to acquire a target through the use of an actuator. In practice, reaction wheels commonly perform this function by producing a reactive torque on the spacecraft. Consequently, due to the static and dynamic imbalances in individual reaction wheels, an undesired vibration, called jitter, is generated during operation and causes variations in the spacecraft's attitude. Focusing on missions and payloads operating in the infrared band, optical jitter effects on target detection and tracking performance need to be investigated.

Using a quaternion error feedback design, jitter produced by the reaction wheels was recorded while performing a standard spacecraft maneuver. Simulating a low earth orbiting satellite, the vibrations generated a significant optical jitter blur due to a line-of-sight motion. After implementing the optical jitter blur in a baseline high resolution image, the simulation considerably reduced the frame's spatial resolution and intensity. The simulation demonstrated the jitter blur's effects on spatial resolution and intensity, which significantly decreased the system's ability to detect and track objects-of-interest.

THIS PAGE INTENTIONALLY LEFT BLANK

TABLE OF CONTENTS

LIST OF FIGURES

LIST OF TABLES

THIS PAGE INTENTIONALLY LEFT BLANK

LIST OF ACRONYMS AND ABBREVIATIONS

AOCOE	Adaptive Optics Center of Excellence
α-Si	amorphous silicon
ATFLIR	advance targeting forward-looking infrared
CdSe	cadmium selenide
DSP	Defense Support Program
FIR	far-infrared
FPA	focal plane array
Ge	germanium
GEO	geostationary earth orbit
HBCRT	High Energy Laser Beam Control Research Testbed
HEL	high energy laser
HgCdTe	mercury cadmium telluride
IR	infrared
InSb	indium antimonide
ISR	intelligence, surveillance, and reconnaissance
LCM	local contrast method
LWIR	long wave infrared
MK	Mark (designation of product version)
MOD	model
MTF	modulation transfer function
MWIR	mid-wave infrared
NIR	near infrared
OPIR	overhead persistent infrared
PbSe	lead selenide
PCA	principle component analysis
QWIP	quantum-well infrared photodetector
SBIRS	Space Based Infrared System
Si	silicon
Si:As	silicon doped with arsenic

SWIR	short-wave infrared
VOx	vanadium oxide

ACKNOWLEDGMENTS

I would like to thank my primary advisor, Professor Jae Jun Kim, for his guidance and assistance in my research. His technical expertise and experience in spacecraft jitter, attitude control, and target tracking was absolutely critical to the completion of this thesis. I would also like to thank my co-advisor, Professor Brij Agrawal, and the staff of the Adaptive Optics Center of Excellence (AOCOE) for always providing the support and equipment needed to conduct my research.

Lastly, I would like to thank my wife, Linh Flores, for taking care of our family and supporting me during my time at the Naval Postgraduate School. I credit my success and give my thanks to these individuals.

THIS PAGE INTENTIONALLY LEFT BLANK

I. INTRODUCTION

Electro-optic and thermal imaging systems for spacecraft contribute to the missions of commercial and government organizations in the fields of meteorology, oceanography, agriculture, forestry, education, surveillance, and intelligence. The performance of these imaging systems is gauged by the resolution that the system is able to provide. Resolution is categorized as spatial, spectral, temporal, or radiometric. As sensory data becomes more critical for missions, electro-optical and thermal systems will be required to provide data with greater resolution at farther distances including outside Earth's atmosphere. While using mechanical systems on imaging spacecraft, undesirable vibrations called jitter occur. Jitter, when significant enough, can be a limiting factor in the resolution of imagery data. Therefore, the reaction wheel's vibration model is critical for designing a complex imaging system. How is jitter integrated into the spacecraft design, and what are its effects on imaging, detection, and tracking performance?

A. MOTIVATION

> U.S. space capabilities will continue to be fundamental for national security. DOD and the IC will identify, improve, and prioritize investments in those capabilities that garner the greatest advantages. We will develop, acquire, field, operate, and sustain space capabilities to deliver timely and accurate space services to a variety of customers, from soldiers to national decision-makers.
>
> —R. Gates and J. Clapper [1]

For U.S. space capabilities, overhead persistent infrared (OPIR) is a critical element that employs sensors in the infrared band, which provides essential data for national decision- and policy-makers. OPIR's role in space force enhancement facilitates reconnaissance, missile tracking, and launch detection [2]. Information gathered from OPIR assets help detect, track, and characterize the adversary's assets. Therefore, it is important to understand the dynamic model of operations in order to assess the performance of OPIR systems.

B. LITERATURE REVIEW

In the early 1990s, NASA started recognizing that spacecraft were driven to larger and lighter structures due restrictions on mass from the launch vehicle, coupled with more capable payloads [3]. Larger and more capable payloads required more stable structures for precise measurements and observations. NASA's Langley Research Center was investing in methods to measure, mitigate, and control jitter effects on structures. In order to validate and mitigate structural vibrations, NASA developed a large suspended structure at Langley Research Center to simulate structures in a zero gravity environment and to observe how vibrations propagated through large structures.

> One of the largest disturbance sources onboard the spacecraft is the reaction wheel. SDO (Solar Dynamics Observatory) carries four wheels to provide 3-axis pointing stabilization. These wheels also generate large tonal and broadband disturbances due to mass imbalances, bearing imperfections, and mechanical noises. The wheel disturbances are difficult to model accurately since their frequency and magnitude change with wheel speeds. They can also interact with wheel structural modes, greatly amplifying their disturbance level.
>
> —K. Liu, P. Maghami, and C. Blaurock [4]

Since the magnitude of the tonal disturbance is proportional to the squared value of the reaction wheel speed, higher wheel speeds created a larger jitter response at a greater frequency [4]. In NASA's analysis, the broadband noise was more apparent at lower reaction wheel speeds and was measured when the tonal disturbance were subtracted. These models have been validated through ground testing and have been essential in constructing systems for active jitter control and setting operation limits for the reaction wheels [4].

A paper written by Lulu Liu from the Massachusetts Institute of Technology discussed the modeling of jitter from a reaction wheel assembly as static or dynamic torque [5]. Then, Liu assessed if the spacecraft can fulfill its pointing accuracy requirement while being subjected to static and dynamic disturbance torques. Lulu Liu's and NASA's jitter model agree that the torque generated are both a function of the squared value of the wheel's angular velocity. Lui's requirement for pointing accuracy

was 2 arcseconds given the characteristics of static and dynamic imbalances in the reaction wheel. Lui's reaction wheel assembly for modeling the jitter consisted of three reaction wheels with their normal-axis in-line with the body's principle axis. Uniform static and dynamic imbalances were modeled from Ithaco Type A reaction wheels and spun at constant revolutions per minute to calculate the linear displacement of the spacecraft's body. Lui's results were that given the spacecraft's mass, locations of reaction wheels, and moments of inertia, the angular displacement were within tolerance to achieve 0.2 arcseconds pointing accuracy.

Previous research by Naval Postgraduate student Michael Krueger in the field of overhead persistent infrared compared the performance of various detection and tracking algorithms [6]. Taking detection data from infrared systems, alpha-beta and Kalman filters were applied to naval scenarios centered on transits in the Strait of Hormuz and tactical small boat swarms. In order to see which algorithm performed better, mean measurement error and track error were recorded during the scenarios for the alpha-beta and Kalman filter. In the effort to test the local contrast method (LCM) and principle component analysis (PCA), noise was incrementally added into the scenes to see its effect on detection performance. By incrementally adding noise, sensor and environmental factors were incorporated in the calculation of probability of detection and probability of false alarms.

The results of Michael Krueger's research found that the local contrast method was a better algorithm for the chosen scenarios because it accounted for the increased signal-to-noise ratio of the target [6]. The drawback of utilizing the LCM is that large static objects in the field-of-view could be seen as targets. While principle component analysis provided a lower number of false alarms, it also lowered the signal-to-noise ratio of the intended target, resulting in a lower probability of detection and decreased overall performance.

C. OBJECTIVES

The objective of this thesis is to construct, implement, and simulate the effects of jitter from an attitude control system and to observe the effects on the accuracy of an

infrared tracking system. Previous work in similar fields constructed models for reaction wheel jitter and modeled the total angular displacement as a function of the reaction wheel's angular velocity. However, previous jitter analysis and OPIR research did not integrate the effects of jitter into target tracking.

By implementing static and dynamic imbalances in reaction wheel assembly, a disturbance torque can be calculated from a spacecraft's maneuvering operations. The disturbance torque caused by jitter affects the results by generating a blur on the sensor's image. Jitter blur results in a decrease in accuracy of tracking systems. Utilizing aerial infrared imagery for simulations, sensor and tracking data are subjected to jitter blur to investigate the effects of vibrations from a reaction wheel attitude control system.

D. OVERVIEW

Chapter II provides the background for infrared space-based capability. This chapter addresses the necessity for space-based capabilities and the advantages of working in the infrared spectrum instead of the visual frequency band. Additionally, Chapter II discusses how the United States Navy currently employs infrared sensors.

Chapter III provides the fundamental concepts and methods used to construct the simulations. Starting with the reaction wheels, jitter is categorized into two types of disturbance torques. The reaction wheel's dynamic model and jitter are a function of the wheel's angular velocity and momentum, which are integrated to an attitude control system. Once jitter has been introduced, the effects of jitter blur and its modulation transfer function (MTF) are discussed. In order to integrate sensor and target tracking capabilities, the Kalman filter and its implementation as an optimal tracking algorithm are described in this chapter.

Chapter IV analyzes the results of a sensor being subjected to jitter. The results are then compared to the non-jitter environment in order to identify the effects that jitter had on target tracking performance.

Chapter V provides a system overview and sensor description of the High Energy Laser (HEL) Beam Control Testbed (HBCRT). The HBCRT is the Naval Postgraduates School's testbed for high energy laser, control, and target tracking applications.

Chapter VI includes the conclusions for this thesis and offers potential topics for future research work.

THIS PAGE INTENTIONALLY LEFT BLANK

II. OPERATING IN THE INFRARED SPECTRUM

This chapter focuses on the operations in the infrared band for the U.S. Navy and U.S. Airforce. These operations are heavily dependent on energy's propagation through the atmosphere. The major effects on radiated energy through the atmosphere are absorption and scattering. Absorption and scattering effects are associated with different atmospheric molecules and particles, which are identified and addressed in this chapter.

A. OVERHEAD PERSISTENT INFRARED MISSION

The primary mission of overhead persistent infrared is the protection of the United States and allied forces from ballistic missile threats. This program encompasses the Defense Support Program (DSP) and the Space Based Infrared System (SBIRS) [7]. In 1970, the DSP program provided an early warning capability for intercontinental ballistic missile detection using infrared payloads.

The SBIRS program is the follow-on to the DSP program as a ballistic missile warning system, which employs geostationary orbit (GEO) satellites and is hosted on highly elliptical orbit (HEO) satellites [7]. With an array of overhead infrared sensors, OPIR systems augment the capabilities of the Remote Sensing Systems Directorate to participate to in Department of Defense (DOD), national security, and scientific missions.

B. ATMOSPHERIC EFFECTS IN THE INFRARED BAND

Imaging sensors can collect radiation in the visible and infrared bands of the electromagnetic spectrum. Regarding the infrared band, infrared sensors are designed to collect radiated energy with wavelengths from $0.7\,\mu m$ to $15\,\mu m$. The wavelength of emission is important because the wavelength determines the type of detector material used in the sensor and the propagation through the atmosphere. This section focuses on the electromagnetic propagation in the infrared wavelengths, which is affected by the atmosphere and environment. The way infrared energy is affected by the atmosphere determines if operating in the infrared band is advantageous compared to the visible

band. The wavelengths and characteristics of the infrared bands are presented in Figure 1 and Table 1.

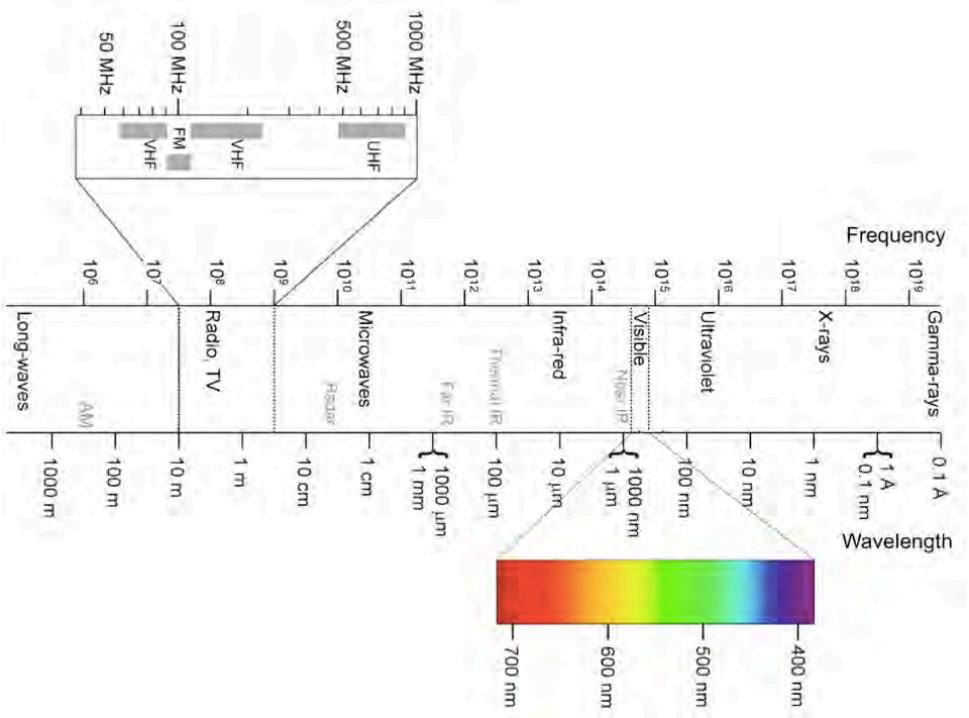

Figure 1. Electromagnetic Spectrum: Bands and Associated Wavelengths

Source [8]: (2013, April 19). *Scalable Neuroscience and the Brain Activity Mapping Project*. Available: http://cs.brown.edu/people/tld/note/blog/13/04/19/

Table 1. Characteristics of Infrared Bands and Detector Materials

IR Segment	Abbreviation	Wavelength (µm)	Frequency (THz)	Detector Material
Near Infrared	NIR	0.7–3.0	100–428	CdSe, Ge, HgCdTe, Si
Mid-Wave Infrared	MWIR	2.5–6	50–120	HgCdTe, InSb, PbSe
Long Wave Infrared	LWIR	7.0–15.0	20–42	α -Si, HgCdTe, QWIP, Si:As, VOx

Adapted from Source [9]: K. Kasunic, *Optical Systems Engineering.* New York: The McGraw-Hill Companies, 2011.

1. Absorption

The constituents and conditions of the atmosphere effect the propagation of electromagnetic energy, and those effects are a function of the energy's wavelength. The effects can be characterized by two types of matter in the air: molecular and aerosol. Both molecules and aerosols absorb radiated energy that result in the decreased intensity value of the receiving sensor.

Absorption occurs when radiation is turned into kinetic energy in the form of heat by a gaseous molecule. The determining factor of whether radiated energy will be absorbed is the molecule's or aerosol's bandgap energy. The molecule's bandgap energy must be lower than the radiated energy in order for absorption to occur. The bandgap energy is determined by the type of molecules present in the medium in which the radiated energy is traveling. Craig Payne explains that the atmosphere is mainly made up of nitrogen and oxygen; however, the water vapor, carbon dioxide, nitrous oxide, carbon monoxide, and ozone are predominant absorbers of radiated energy [10]. From a remote sensing perspective, Figure 2 exhibits the absorption bands and atmospheric windows. The molecules in the atmosphere create bandgaps where energy is highly absorbed and reflected. From *Principles of Naval Weapon Systems,* the molecules that produce the bandgaps are typically water vapor, carbon dioxide and oxygen. Outside of the bandgaps, transmission windows particularly in the 0.7–1.2, 3–6, and 8–13 μm wavelength have a high transmission percentage [10].

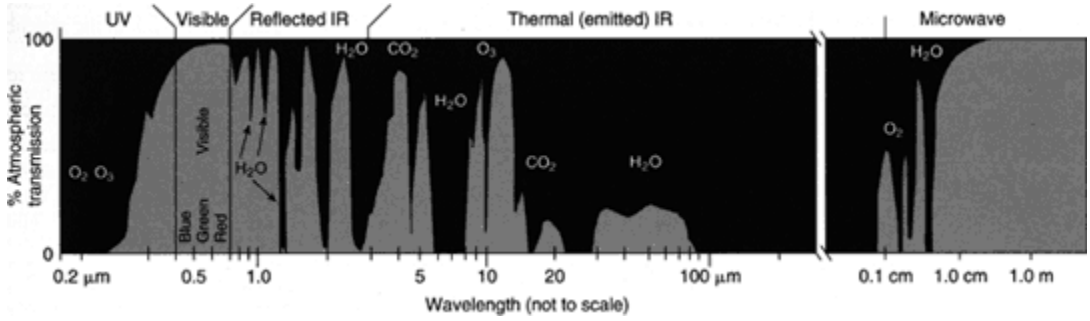

Figure 2. Atmospheric Transmission Windows

Source [10]: C. Payne, *Principles of Naval Weapon Systems.* Annapolis, MD: United States Naval Institute, 2010.

2. Scattering

Scattering is the deflection of electromagnetic radiation due to atmospheric particles. The deflection is characterized by the ratio between the particles in the air and the wavelength of the radiated photons (see Table 2). The three types of scattering are Rayleigh, Mie, and geometric optical [10]. Rayleigh scattering takes place when the particle size is significantly smaller than the traveling energy's wavelength. Mie scattering occurs when the wavelength is about the same size of the particle radius. Geometric optical scattering occurs when the particles are much larger than the wavelength [10]. Since the visible light band is 0.4–0.7μm in wavelength, the infrared spectrum is advantageous when operating in the hazy environment where the effects of Rayleigh scattering are minimal and particles are below 1μm.

Table 2. Atmospheric Particles

Particle Type	**Radius (μm)**	**Density (per cm^3)**
Air molecule (Rayleigh)	10^{-4}	10^{-4}
Haze Particles (Rayleigh)	$1\times10^{-2}-1.0$	$10-10^{3}$
Fog Droplet (Mie)	$1.0-10$	$10-100$
Raindrops (geometric)	$10^{2}-10^{4}$	$10^{-5}-10^{-2}$

Source [10]: C. Payne, *Principles of Naval Weapon Systems.* Annapolis, MD: United States Naval Institute, 2010.

Aerosols are particulates in the atmosphere that absorb and scatter radiated energy. The source of aerosols fall within three main categories: volcanic aerosols, desert dust, and man-made aerosols [11]. From volcanic eruptions, a layer of sulfur dioxide gas is formed in the stratosphere, which is able to scatter and absorb radiation. The second type of aerosol is desert dust [11]. Desert, or mineral, dust absorbs and scatters radiation causing the surrounding air to heat up. The heat produced by the mineral dust creates atmospheric turbulence and varying refractive properties. The third type of aerosol is man-made. Man-made aerosols are generated from burning coal, oil, and timber [11]. Sulfate aerosols reflect optical energy but do not absorb it.

The near infrared and long wave infrared bands experience less Mie scattering effects, making them advantageous in hazy environments. Additionally, in a foggy setting, Rayleigh scattering does not play a major factor in the propagation of infrared energy. In these two environments, infrared sensors possess performance advantages over visible band sensors. Figure 3 depicts the performance advantages of imagery in the infrared band over the visible band in various environments.

Figure 3. Scattering Effects of Smoke, Fog, and Atmospheric Obscurants in the Visible and Infrared Bands

Source [12]: *With Infrared, Military Owns More Than the Night*. Available: http://www.photonics.com/Article.aspx?AID=53438

C. U.S. NAVY UTILIZATION OF INFRARED BAND

The U.S. Navy employs a wide array of infrared sensors in support of its operations. In the infrared spectrum, there are two types of sources in which the Navy is interested: selective and thermal [10]. Described in *Principles of Naval Weapon Systems*, a selective source emits energy in a narrow band of energy such as an exhaust plume or

rocket engine, whereas a thermal source emits a broadband of energy and its peak wavelength is a function of its temperature.

Due to the atmospheric windows and Wien's displacement, 3–5 and 8–12 μm infrared sensors are employed on military systems [10]. In *Principles of Naval Weapon Systems*, Payne pairs thermal and selective sources with their emission wavelength. Personnel and vehicles are approximately 27 degrees Celsius, which is best measured by long wave infrared sensors at 8–12 μm. Jet's plume and exhaust temperature range from 100 to 1,000 degrees Celsius making midwave infrared sensors the suitable choice to search for this type of target. In an aircraft's plume, water vapor and carbon dioxide are selective emitters at a wavelength of 4.3 μm due to the high exhaust temperatures. To characterize the detection, Payne notes that the analysis on the plume emissions aids in determining the type of fuel used by a projectile. Spikes on the spectral emittance can help determine the fuel ratio used in combustion [10]. Spectral spikes in Figure 4 exemplify the wavelengths of emission and radiance from a typical plume.

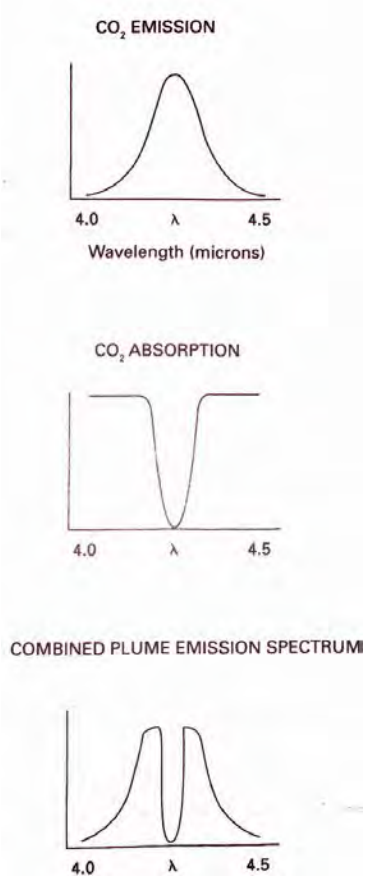

Figure 4. Exhaust Plume Spectrum

Source [10]: C. Payne, *Principles of Naval Weapon Systems.* Annapolis, MD: United States Naval Institute, 2010.

Skin temperatures through aerodynamic heating and environmental heating also emit for targets of interest emission in the infrared spectrum. At a speed of approximately of Mach 0.7, the skin of projectiles is raised to 24 degrees in laminar flow regions [10].

For ground targets, emissions in the infrared band are commonly generated from three different sources: combustion, friction, and environmental sources [10]. The following definitions of each these sources are provided from *Principles of Naval Weapon Systems*. Combustion results in a release of energy that transfers heat to the exhaust components and plume. Frictional heat is a resultant from using mechanical and transmission systems. Lastly, environmental sources transfer energy from surrounding sources (such as the sun) to the target. Since the characteristics of emissions and temperature are significantly different that the natural background, the target stands out

from natural background. Table 3 provides a brief overview of reflection and emission sources that are commonly used for infrared detection in the air and surface environment.

Table 3. Thermal Radiation Sources

Reflection Sources	Emission Sources
• Solar • Sky • Earth • Hot parts off body • Plume off body	• Skin • Plume (spectral) • Hot parts

Source [10]: C. Payne, *Principles of Naval Weapon Systems.* Annapolis, MD: United States Naval Institute, 2010.

Figure 5 is the MK46 MOD1 Optical Sight System that is currently being deployed on U.S. Navy Arleigh Burke-class destroyers to aid situational awareness for surface and air targets. The MK46 MOD 1 is capable of imaging in the infrared spectrum at 3–5 and 8–12 micrometers [13].

Figure 5. MK 46 MOD1 Optical Sight System

Source [13]: (2008, April 7). *MK46 MOD1 Optical Sight System*. Available: http://www2.l-3com.com/keo/pdfs/AD39%20MK46%20MOD%201%20datasht.pdf

Figure 6 is a depiction of the AN/SQ-228 ATFLIR EO/IR sensor, which is integrated on F/A-18 Hornets. The ATFLIR system's mission is to provide navigation and targeting information during adverse weather conditions and is used as a laser spot tracker.

Figure 6. AN/SQ-228 Advanced Targeting Forward Looking System

Source [14]: *Advanced Targeting Forward Looking Infrared [ATFLIR]*. Available: http://www.raytheon.com/capabilities/products/atflir/

1. Detect-to-Engage Sequence

Precise tracking is critical to any guided weapon or intelligence, surveillance and reconnaissance (ISR) payload. Tracking is the resultant of a culmination of steps that include target detection, localization, and classification. These steps are part of the initial process for the Navy's basic fire control problem [10]. Summarizing the detect-to-engage sequence, a system detects and tracks a target, selects the appropriate weapon, and neutralizes the target [10]. This section identifies and discusses the shared processes between the detect-to-engage sequence and OPIR tracking.

The first common process is detection. Detection means to actively or passively confirm the presence of a target of interest within the system's field-of-regard [10]. *Principles of Naval Weapon Systems* identifies two types of detection methods: active and passive. Active detection process sends energy out, usually in the form of radar or lasers, and discovers a target from the energy's return. Passive detection is searching for an object-of-interest by looking at its emittance in a particular wavelength.

Once detected, a sensor system is able to provide information on a target's location. Sufficient location information is gathered either through a series of measurements or single a frame depending on the sensor type [10]. The process of determining the target's position relative to the sensor is called localization. The precision of the location information is based on the resolution of the sensor, range to the target, and the accuracy of the line-of-bearing to the target.

As in OPIR tracking, classification of the target is an important step during the detect-to-engage sequence. It defines the dynamic model for the tracking algorithm. If the target's classification is incorrect, the wrong dynamics models is selected and provides a poor estimation of the target's location. Each of these errors deducts from the estimator's performance and reduces the mission effectiveness of the regarded weapons or ISR system.

Error is introduced into the process as sensor noise during the detection and localization process. Noise can be defined as any signal that is not of interest and unwanted that is coupled to the target or sensor [10]. Noise can come from background radiation sources or be self-induced by the sensor. This could inhibit the sensor system from providing precise target data for any one of the three steps mentioned.

Today, adversaries' vehicles and weapon systems are developed to avoid detection and to be difficult to track. These systems utilize the background and hide in surrounding clutter and noise. Additionally, the adversary's operational maneuvers are complex making the tracking system's dynamic model inaccurate. Coupled with high speeds, a stealthy and maneuverable target would be difficult to track precisely.

The estimation and tracking process is critical for the detect-to-engage sequence and OPIR scenarios. Utilizing sensor data and dynamic model, estimation and tracking results are incorporated in a fire control solution. Although the principles in this thesis focus on OPIR scenarios, the principles are applicable to many naval sensor and weapons systems.

III. CONCEPTS AND GROUNDWORK FOR SIMULATION

This chapter lays out the main concepts and methods used in developing the simulation. The initial topics covered in the chapter are reaction wheels and the disturbances they induce while in operation. Next, the integration of reactions wheels into a spacecraft attitude control system design is covered. Given a desired attitude maneuver, the amount of jitter generated from the reaction wheels can be estimated. Using the attitude data from the simulation's maneuver, the modulation transfer function for optical jitter is used on a sample of infrared imagery. By means of the Kalman filter, targets are detected and tracked in the sample infrared imagery with jitter blur added. The methods and processes mentioned are presented in the following sections.

A. SPACECRAFT REACTION WHEEL OPERATION

An attitude control system uses reaction wheels to orient the spacecraft and stores momentum to stabilize the spacecraft from disturbance torques. Figure 7 is an example of commercial reaction wheel hardware for small satellites. While OPIR platforms utilize lighter structural materials to reduce the overall mass, internal mechanical devices, such as reaction wheels, cause vibrations to the system that affect the projection onto the focal plane array (FPA). The attitude oscillation of the spacecraft platform is known as jitter.

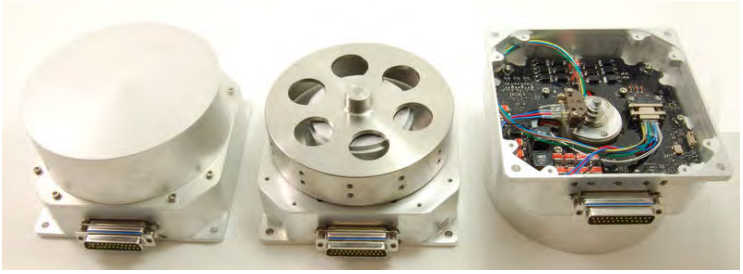

Figure 7. Clyde Space Small Satellite Reaction Wheel

Source [15]: *Small Satellite Reaction Wheels*. Available: http://www.clyde-space.com/products/reaction_wheels

1. Static Unbalance

Jitter from reaction wheels can be categorized into two types: static and dynamic. Static jitter is the uneven distribution of mass radially in the wheel [5]. The force vector is a function of time, and the maximum magnitude is determined by the static imbalance and the wheel speed. For a spacecraft attitude control system, three reaction wheels are aligned with the *x*-axis for roll, *y*-axis for pitch, and *z*-axis for yaw. The force imparted by the radial imbalance is directly proportional to the reaction wheel's angular velocity (see Equation 3.1) [5]. These static forces are a sum of components that induce a torque when applied off the center of mass (see Equation 3.2) [5].

$$\begin{aligned}\vec{F}_s(\omega_x,\omega_y,\omega_z) = &(S_y\omega_y^2\sin(\omega_y t+\varphi_y)+S_z\omega_z^2\cos(\omega_z t+\varphi_z))\hat{x}\\ &+(S_z\omega_z^2\sin(\omega_z t+\varphi_z)+S_x\omega_x^2\cos(\omega_x t+\varphi_x))\hat{y}\\ &+(S_x\omega_x^2\sin(\omega_x t+\varphi_x)+S_y\omega_y^2\cos(\omega_y t+\varphi_y))\hat{z}\end{aligned} \tag{3.1}$$

$$\vec{\tau}_s(\omega_x,\omega_y,\omega_z) = \vec{R}_w \times \vec{F}(\omega_x,\omega_y,\omega_z) \tag{3.2}$$

The attitude control system for the simulation consists of a fourth reaction wheel that was placed off the principle axis to provide redundancy in the case of a reaction wheel failure. To translate the effects of the force generated by the fourth reaction wheel, body-axis rotations were used by applying directional cosine matrices (DCMs) [16]. For the simulation's attitude control system, Equation 3.3 represents the rotation about the *y*-axis and Equation 3.4 represents the rotation about the *z*-axis [16]. By multiplying the two directional cosine matrices, the force vector is calculated given the orientation of the reaction wheel in θ_1 and θ_2 in Equation 3.5.

$$C_1(\theta_1) = \begin{bmatrix} \cos(\theta_1) & 0 & \sin(\theta_1) \\ 0 & 1 & 0 \\ -\sin(\theta_1) & 0 & \cos(\theta_1) \end{bmatrix} \tag{3.3}$$

$$C_2(\theta_2) = \begin{bmatrix} \cos(\theta_2) & -\sin(\theta_2) & 0 \\ \sin(\theta_2) & \cos(\theta_2) & 0 \\ 0 & 0 & 1 \end{bmatrix} \tag{3.4}$$

$$\begin{bmatrix} \vec{b}_1 \\ \vec{b}_2 \\ \vec{b}_3 \end{bmatrix} = C_1(\theta_1)C_2(\theta_2)\begin{bmatrix} \vec{a}_1 \\ \vec{a}_2 \\ \vec{a}_3 \end{bmatrix} \tag{3.5}$$

As a result of the forces from all the reaction wheels, torques are produced on the body of the spacecraft. This torque is calculated with the cross product of the distance from the center of mass and the amount of static force applied [5].

2. Dynamic Unbalance

Dynamic jitter is caused by the uneven distribution of mass of the wheel that is tangential to the spin plane [5]. The variance of mass that resides in the wheel will gravitate toward the spin plane, resulting in unwanted torque on the spacecraft. The resultant torque is a direct byproduct of the dynamic imbalance and is not dependent on the distance between the wheels and the center of mass [5]. Equation 3.6 is the expression for the torque exerted on the spacecraft due to dynamic jitter [5].

$$\begin{aligned} \vec{\tau}_d(\omega_x,\omega_y,\omega_z) = &(\mathrm{D}_z\,\omega_z^2\sin(\omega_z t+\phi_z')+\mathrm{D}_y\,\omega_y^2\sin(\omega_y t+\phi_y'))\hat{x} \\ &+(\mathrm{D}_x\,\omega_x^2\sin(\omega_x t+\phi_x')+\mathrm{D}_z\,\omega_z^2\sin(\omega_z t+\phi_z'))\hat{y} \\ &+(\mathrm{D}_y\,\omega_y^2\sin(\omega_y t+\phi_y')+\mathrm{D}_x\,\omega_x^2\sin(\omega_x t+\phi_x'))\hat{\mathrm{z}} \end{aligned} \tag{3.6}$$

To analyze the torque from of the fourth reaction wheel, two axial rotations were applied similarly in the case of static jitter. Applying two directional cosine matrices, the equation to calculate the torque from the fourth reaction wheel is

$$\begin{bmatrix} \tau_1 \\ \tau_2 \\ \tau_3 \end{bmatrix} = C_1(\theta_1)C_2(\theta_2)\begin{bmatrix} D_4\omega_4^2\sin(\omega_4 t+\phi_4') \\ -D_4\omega_4^2\sin(\omega_4 t+\phi_4') \\ 0 \end{bmatrix} \tag{3.7}$$

B. JITTER BLUR

The angular displacements from the reaction wheels' disturbance torque affect the optical system's line-of-sight (LOS). In Equation 3.8, the total image blur is the sum of

optical, atmospheric, and jitter blur[9]. The tilting and decentering of the optical path, are categorized as jitter blur, θ_j. Jitter blur is one of the components of the overall blur, θ. θ_a is atmospheric blur, and θ_o is optical blur in Equation 3.8 [9].

$$\theta = (\theta_o^2 + \theta_j^2 + \theta_a^2)^{1/2} \tag{3.8}$$

Equation 3.9 is the modulation transfer function (MTF) that expresses the response of an image from jitter as a function of the frequency and angular displacement [9]. The MTF assumption is that the jitter frequency is higher than the sample rate of the system. When the jitter frequency is greater than the frame rate, target blurring occurs on the radiation source since the object is moving during the FPA's exposure time [9]. In Equation 3.9, the variable f is the frequency in cycles per radian.

$$MTF_j = \exp\{-2(\pi\theta_j f)^2\} \tag{3.9}$$

C. ANGULAR MOTION OF TELESCOPIC SENSOR

For the simulation, the imaging sensor is mounted on the spacecraft through a gimbal. The gimbal enables the sensor to move its field of view to the area of interest. Assuming a one dimensional and proportional derivative control for the gimbal, the spacecraft's platform jitter relationship with the telescopic sensors line-of-sight is expressed though Equations 3.10 and 3.11 [16]. J_T is the moment of inertia of the telescope, K_p is the proportional term, and K_d is the derivative term.

$$J_T\ddot{\theta}_T = -K_p(\theta_T - \theta_S) - K_d(\dot{\theta}_T - \dot{\theta}_S) \tag{3.10}$$

$$J_T\ddot{\theta}_T + K_d\dot{\theta}_T + K_p\theta_T = K_p\theta_S + K_d\dot{\theta}_S \tag{3.11}$$

Figure 8 is a graphic depiction of the gimbaled telescope mounted on the spacecraft. θ_S is the angular disturbance of the spacecraft orientation due to the imbalance of the reaction wheels. θ_T is the line-of-sight angle of the optical telescope.

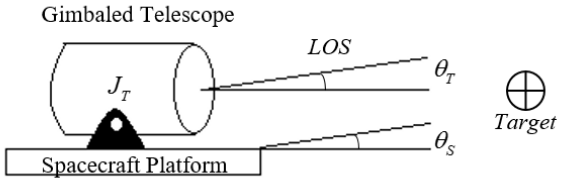

Figure 8. Depiction of Angular Motion Terms of Telescope

D. ATTITUDE CONTROL SYSTEM

The attitude control system (ACS) orients the spacecraft's body to the desired state through the use of an actuator. For this thesis, actuators are reaction wheels that produce a force by changing its momentum and inducing a torque around the center of mass which cause the spacecraft to rotate and orient its body to the desired attitude.

The configuration of the attitude control system is a tetrahedron. Three reactions wheels are each aligned with the principle axis while the fourth is rotated 45 degrees along the pitch axis (*y*-axis) and rotated again 45 degrees along the yaw axis (*z*-axis). The purpose of the fourth reaction wheel is to increase the reliability of the ACS in the case of reaction wheel failure. Figure 9 exhibits reaction wheels oriented in a tetrahedron configuration. Figure 10 illustrates the reaction wheels' momentum direction where the momentum can change in magnitude through controlling the angular velocity of the wheel [17].

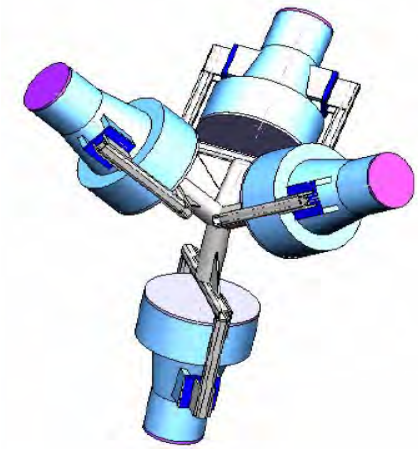

Figure 9. Tetrahedron Reaction Wheel Configuration

Source [17]: (2004). *Satellite Attitude Control System Design Using Reaction Wheels*. Available: auohio.edu/simond/pubs/Gouda04.pdfcademic.cs

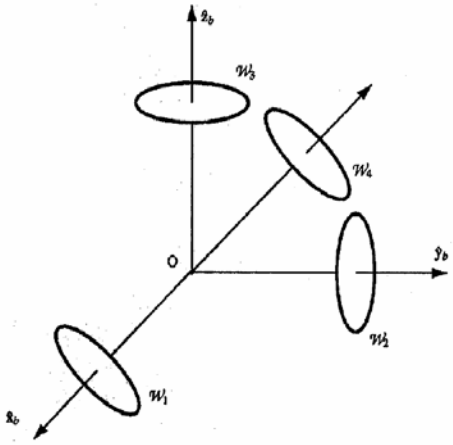

Figure 10. Reaction Wheel Momentum Vectors

Source [17]: (2004). *Satellite Attitude Control System Design Using Reaction Wheels*. Available: auohio.edu/simond/pubs/Gouda04.pdfcademic.cs

1. Quaternion Error Feedback Control System

To develop a control system for the spacecraft, the spacecraft's dynamic model must be estimated and constructed. Equations 3.12 to 3.14 are the attitude dynamics equations to calculate the state (A) and input/control (B) matrices for the state space (see Equation 3.15) [18]. The angular accelerations and velocities in respect to the roll, pitch,

and yaw axis are determined by moving the remaining terms to the other side in Equation 3.16. The process generates six output states in an array from the states space equation.

$$T_x = J_x\ddot{\alpha}_x + (-J_x + J_y - J_z)\omega_0\dot{\alpha}_z + 4(J_y - J_z)w_0^2\alpha_x \tag{3.12}$$

$$T_y = J_y\ddot{\alpha}_y + 3(J_x - J_z)w_0^2\alpha_y \tag{3.13}$$

$$T_z = J_z\ddot{\alpha}_z + (-J_y + J_z - J_x)\omega_0\dot{\alpha}_x + 4(J_y - J_x)w_0^2\alpha_z \tag{3.14}$$

$$\dot{x}(t) = Ax(t) + Bu(t) \tag{3.15}$$

$$\begin{bmatrix} \dot{\alpha}_x \\ \dot{\alpha}_y \\ \dot{\alpha}_z \\ \ddot{\alpha}_x \\ \ddot{\alpha}_y \\ \ddot{\alpha}_z \end{bmatrix} = \begin{bmatrix} 0 & 0 & 0 & 1 & 0 & 0 \\ 0 & 0 & 0 & 0 & 1 & 0 \\ 0 & 0 & 0 & 0 & 0 & 1 \\ \frac{-4(J_y - J_z)w_0^2}{J_x} & 0 & 0 & 0 & 0 & \frac{-(-J_x + J_y - J_z)\omega_0}{J_x} \\ 0 & \frac{-3(J_x - J_z)\omega_0^2}{J_y} & 0 & 0 & 0 & 0 \\ 0 & 0 & \frac{-(J_y - J_x)\omega_0^2}{J_z} & \frac{-(-J_y + J_z + J_x)\omega_0}{J_z} & 0 & 0 \end{bmatrix} \begin{bmatrix} \alpha_x \\ \alpha_y \\ \alpha_z \\ \dot{\alpha}_x \\ \dot{\alpha}_y \\ \dot{\alpha}_z \end{bmatrix} + \begin{bmatrix} 0 & 0 & 0 \\ 0 & 0 & 0 \\ 0 & 0 & 0 \\ \frac{1}{J_x} & 0 & 0 \\ 0 & \frac{1}{J_y} & 0 \\ 0 & 0 & \frac{1}{J_z} \end{bmatrix} \begin{bmatrix} T_x \\ T_y \\ T_z \end{bmatrix} \tag{3.16}$$

After deriving the state space equations, a linear quadratic regulator in conjunction with quaternion error feedback is used for optimization and balance between control error and effort. The balance and level of the control error and effort is determined by the weighing matrices *Q* and *R* (see Equation 3.17 and 3.18) [18]. The terms α and β determine the diagonal value of the weighting matrices and are implemented in the minimization of the cost function in Equation 3.19 [18].

$$Q = diag[...\left(\frac{\alpha_i^2}{x_{i\max}^2}\right) \tag{3.17}$$

$$R = diag[...\left(\frac{\beta_i^2}{u_{i\max}^2}\right) \tag{3.18}$$

$$J = \int_0^\infty (x^T Qx + u^T Ru + 2u^T Nx)dt \tag{3.19}$$

The Simulink block diagram for the spacecraft's attitude control system. Is depicted in Figure 11. From the quaternion error feedback block, the required torque is calculated resulting in commanded angular speed for the reaction wheels. The angular

speed is coupled with the reaction wheel disturbance torque MATLAB function block which generates and inputs the static and dynamic torque into the spacecraft's dynamic system.

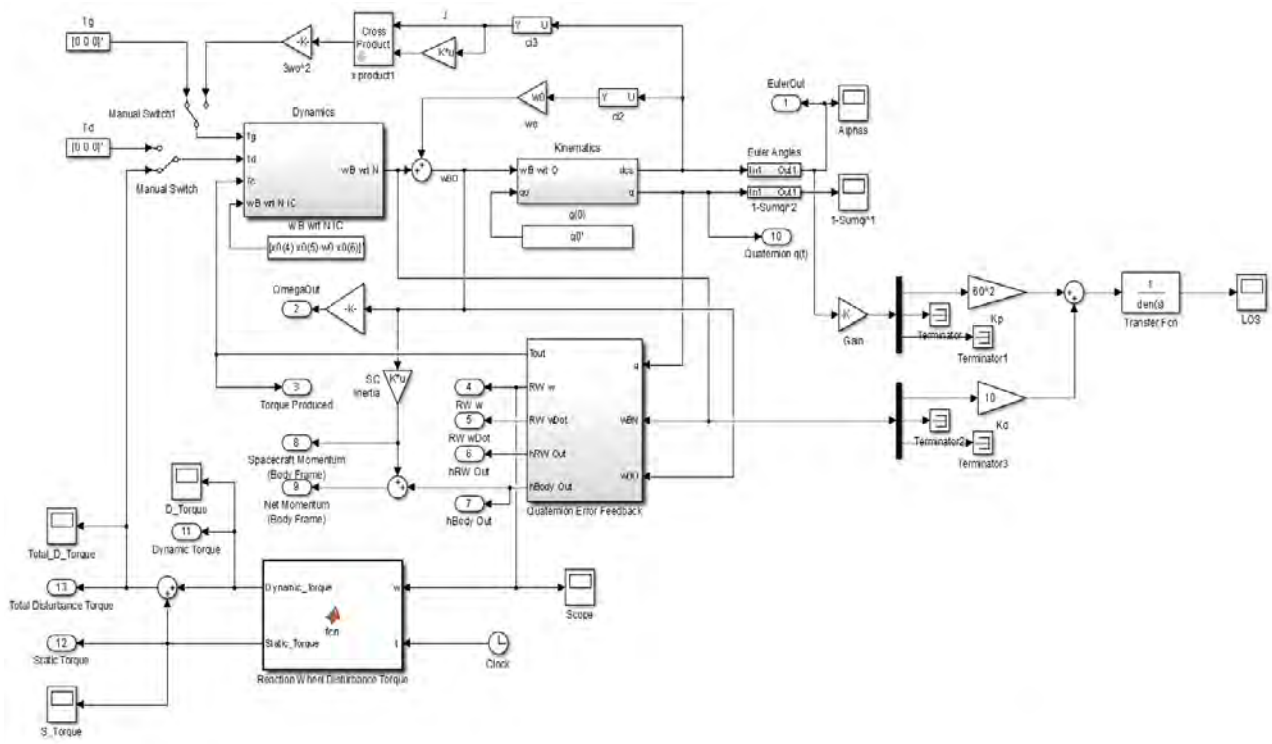

Figure 11. Simulink Block Diagram for Attitude Control System Utilizing Quaternion Error Feedback

E. TARGET DETECTION AND TRACKING

1. Centroid Algorithm

Depending on the field-of-view, resolution, and size of the target, a single target can occupy multiple pixels that exceed the threshold level. The setup in Figure 12 presents the target in a sensor's focal plane in two axes.

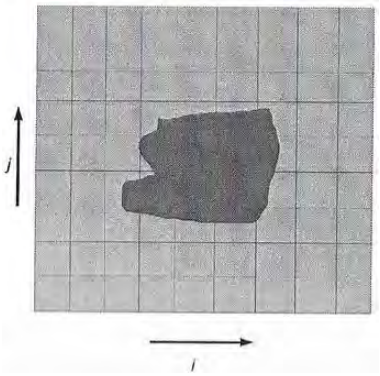

Figure 12. Focal Plane with Target Detection

Source [19]: P. Merrit, *Beam Control for Laser Systems.* Albuquerque, NM: The Directed Energy Professional Society, 2012.

To provide a sensor measurement for the tracking algorithm, the target's position must be calculated. There are three different types of centroid algorithms that provide the positon during the detection process [19]. In *Beam Control for Laser Systems*, Paul Merritt presents three centroid algorithms that are differentiated through their detection threshold levels. For the first algorithm, binary clips the intensity value at the threshold making the detection values a "1" and the background values a "0." Type I maintains the intensity value while including the threshold value. Type II subtracts the threshold value from the detection values and zeros out the remaining values. Figure 13 visually explains the three types of centroid algorithms.

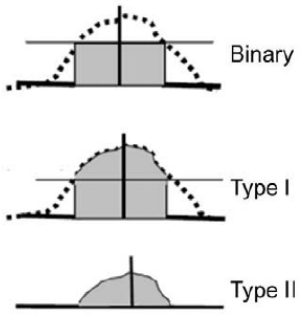

Figure 13. Binary, Type I, and Type II Thresholds for the Centroid Tracking Algorithm

Source [20]: P. Merrit, *Beam Control for Laser Systems.* Albuquerque, NM: The Directed Energy Professional Society, 2012.

In this thesis, binary thresholds are used for the determination of target locations. Bounding box is placed on the potential targets using MATLAB's "regionprops" function.

2. Kalman Filter

Tracking is the estimation of a target's current and future state based on its dynamic model and sensor measurements. For the simulation, the states are position and velocity. A system's dynamic model represents the behavior of a target with respect to time and its input. A common example is the state equation below that represents an object's position with respect to time and acceleration as in Equation 3.20 [20].

$$x(k) = \begin{bmatrix} 1 & T \\ 0 & 1 \end{bmatrix} x(k-1) + \begin{bmatrix} T^2/2 \\ T \end{bmatrix} u(k-1) \tag{3.20}$$

The variable, $x(k)$, represents the state at a particular iteration. In this example, the state represents the target's position and velocity. T represents a discrete amount of time. Acceleration, u, is the input to the dynamics allowing for the target to accelerate. By applying these basic principles and supplementing the tracking process with sensor data, a prediction of the target's future position can be calculated.

Sensor measurements contain errors in the form of sensor noise and inaccuracy's in the dynamic model. In order to mitigate the effects caused by the errors, filtering techniques are applied in order to provide accurate state estimates despite the measurement and process noise present in the process.

The Kalman filter is a sequential tracking and filtering technique that commonly used for estimation processes. For purposes of this thesis, a discrete time method is employed, which is related to the sensor's frame rate.

Inside the Kalman filter, the gain, $W(k+1)$, indicates of the accuracy of the state prediction [20]. From *Estimation with Applications to Tracking and Navigation*, if the state prediction error is large, which is the difference between the true and estimated position, then the Kalman gain will be large. If the measurement residual is large, the

Kalman gain will be small. In other words, the gain sets the sensitivity of the measurement's impact for updating state the equations. It is important to note the assumptions of the Kalman filter that both process and measurement noise are mutually uncorrelated, zero mean, and the covariance matrices are known (see Equations 3.21 to 3.27) [20].

$$E[x(0)v(k)'] = 0 \tag{3.21}$$

$$E[x(0)w(k)'] = 0 \tag{3.22}$$

$$E[v(k)w(j)'] = 0 \tag{3.23}$$

$$E[v(k)] = 0 \tag{3.24}$$

$$E[v(k)v(j)'] = Q(k)\delta_{kj} \tag{3.25}$$

$$E[w(k)] = 0 \tag{3.26}$$

$$E[w(k)w(j)'] = R(k)\delta_{kj} \tag{3.27}$$

For implementation of the Kalman Filter, the state matrix was defined to be

$$A = \begin{bmatrix} 1 & \Delta t & 0 & 0 \\ 0 & 1 & 0 & 0 \\ 0 & 0 & 1 & \Delta t \\ 0 & 0 & 0 & 1 \end{bmatrix} \tag{3.28}$$

Table 4 provides a list of variables used in the Kalman filter and their meanings.

Table 4. Variable Definitions for the Kalman Filter

Variable	Meaning
$x(k)$	Current State Vector
$u(k)$	Known Control Input Vector
t_k	Current Time Step
$x(k+1)$	Predicted State Vector
$F(k)$	State Matrix
$G(k)$	Input Matrix
$v(k)$	Process Noise
$w(k)$	Measurement Noise
$H(k+1)$	Measurement Matrix
$z(k+1)$	Predicted Measurement
$P(k+1\|k)$	State Predicted Covariance
$S(k+1)$	Measurement Prediction Covariance
$W(k+1)$	Filter Gain
$P(k+1\|k+1)$	Updated Covariance

Adapted from [20]: Y. Bar-Shalom, L. Xi and T. Kirubarajan, "Estimation with Applications to Tracking and Navigation," 2001.

Because we are only interested in in the position values of measurement, the measurement matrix, H, is defined as

$$H = \begin{bmatrix} 1 & 0 & 0 & 0 \\ 0 & 0 & 1 & 0 \end{bmatrix} \tag{3.29}$$

From this, the measurement residual is calculated using

$$v(k+1) = z(k+1) - \hat{z}(\mathrm{k}+1|k) \tag{3.30}$$

With the measurement data and the prediction model, the accuracy of the model is described with the covariance matrix in Equation 3.31 [6]. σ_x and σ_y are variances of the residuals between the predicted and model for each axis. The assumption in this research is that σ_x and σ_y are uncorrelated σ_{xy} zero.

$$R_k = \mathrm{cov}(\upsilon_k) = \begin{bmatrix} \sigma_x^2 & \sigma_{xy} \\ \sigma_{xy} & \sigma_y^2 \end{bmatrix} \tag{3.31}$$

The following equation is used to update the state estimate [20].

$$\hat{x}(k+1|k+1) = \hat{x}(\mathrm{k}+1|k) + W(k+1)v(k+1) \tag{3.32}$$

To initiate the Kalman filter process in the simulation, two detections in sequential frames must be within close proximity in order to associate the detections and initiate tracks. At least two detections are required in order to establish the tracks velocity. This velocity is implemented into the dynamics model, which provides an estimation on the track's future position. In the same way, dropping tracks is made when a track has no associated data in two successive frames. Figure 14 is a graphic depiction of the Kalman filter process.

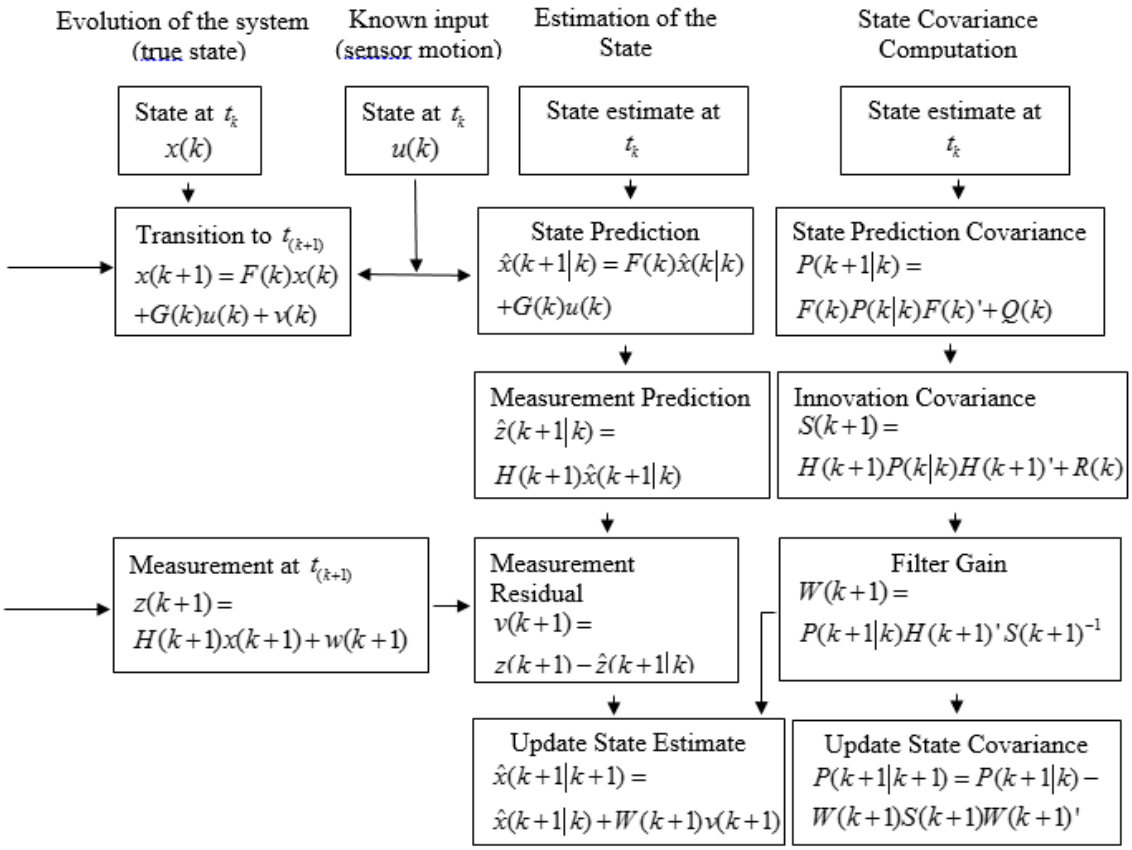

Figure 14. Cycle Flow Chart for the Kalman Filter

Source [20]: Y. Bar-Shalom, L. Xi and T. Kirubarajan, "Estimation with Applications To Tracking and Navigation," 2001.

IV. OVERHEAD PERSISTENT INFRARED SIMULATION

This chapter utilizes the concepts from the previous chapter and presents the simulation results that enabled the analysis of optical jitter effects on target detection and tracking. The simulation's first goal was to determine the attitude oscillation that is caused by the operation of reaction wheels. Next, optical jitter blur from the oscillations were inserted into an image frame with the purpose of examining effects on detection and tracking performance.

A. SIMULATION JITTER

After inputting the Euler Angle of [0, 0, 0] for the desired attitude into the simulation, the commanded angular velocity of the four reaction wheels maintained the spacecraft's attitude despite the external disturbance torques. Figure 15 displays the spacecraft's attitude at the resolution of 0.1 milliradians. However, if the resolution is increased to 0.1×10^{-6} radians, the data shows that the unwanted torque caused variations and oscillations in the spacecraft's attitude, which seen in Figure 16. By sampling the Euler angle simulation data, the attitude's standard deviation during the sensor's sample time provided the information needed for the jitter blur's modulation transfer function.

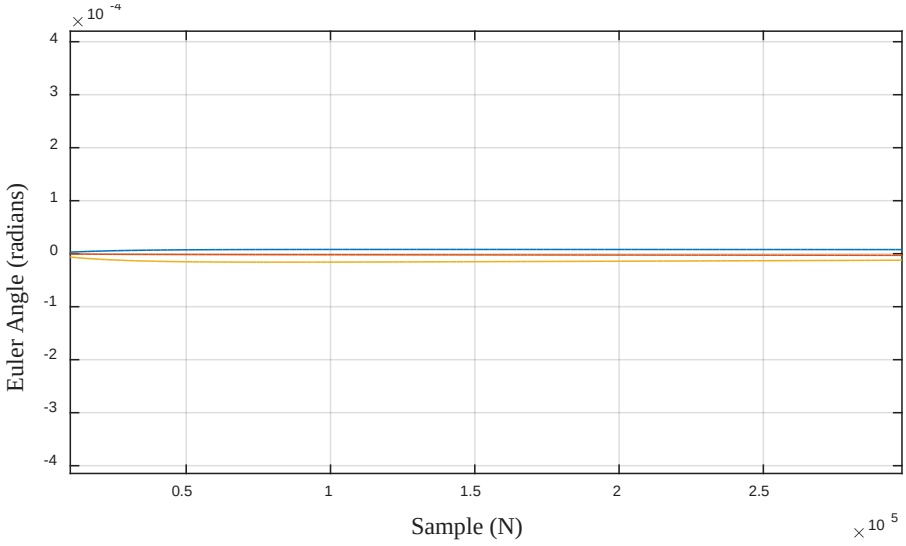

Figure 15. Simulation Results for Spacecraft Attitude

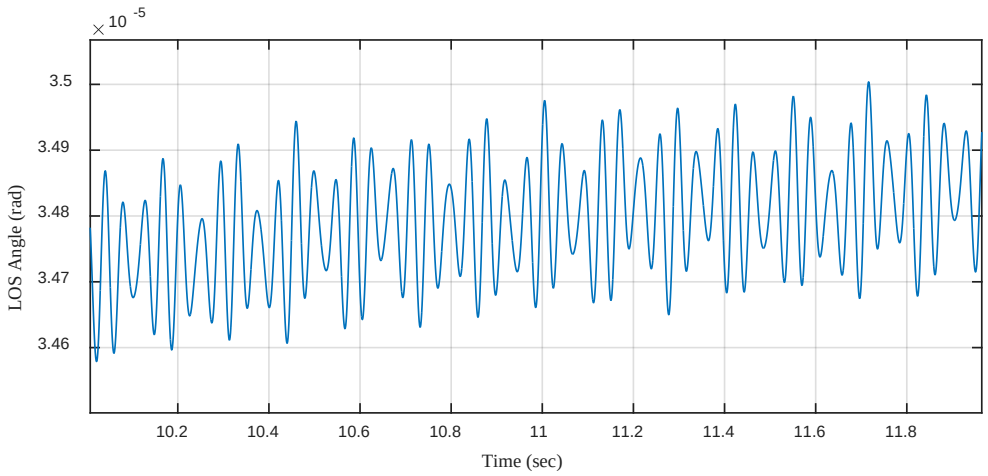

Figure 16. Jitter Caused by Reaction Wheels Operation

The value of the oscillation's standard deviation was 5.97×10^{-6} radians. By multiplying the standard deviation with altitude of the spacecraft (701 kilometers), the sensor's line-of-sight motion on the target resulted in 4.185 meters. The line-of-sight motion becomes greater as the operational altitude increases.

B. IMAGE JITTER BLUR

A color infrared (CIR) image of Boston Logan International Airport in Massachusetts was selected from the National Aerial Photography Program [21]. The selected high definition image served as the baseline, which is shown in Figure 17. Because of the aerial photo's high resolution compared to a remote sensing satellite, the effects of jitter during sensor operation are more apparent for analysis. The baseline image's height is 3,033 pixels in length while the width measures at 3,360 pixels. With an image scale of 1:40,000 and an image resolution of 600 dpi, the resolution is 66.67 inches per pixel or 1.693 meters pixel. In Figure 17, the image is centered on the airport terminal, which consists of multiple airplanes and structures that should exceed the intensity threshold for detection.

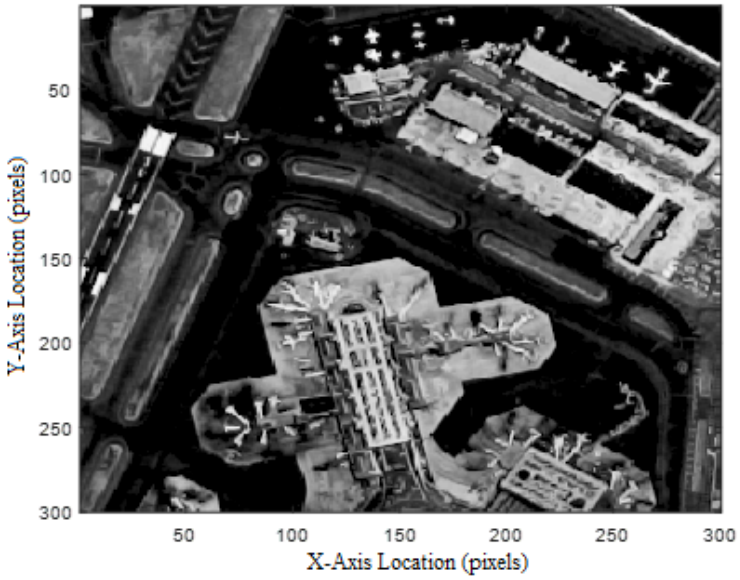

Figure 17. Baseline High Definition Overhead Image (Terrestrial)

Sensor data contains noise that affecst the ability to differentiate between the target and the background. The noise comes from target's background, atmospheric environmental, and thermal noise from the sensor. To make the image more practical, noise was inserted into frame assuming a normal distribution (see Figure 18).

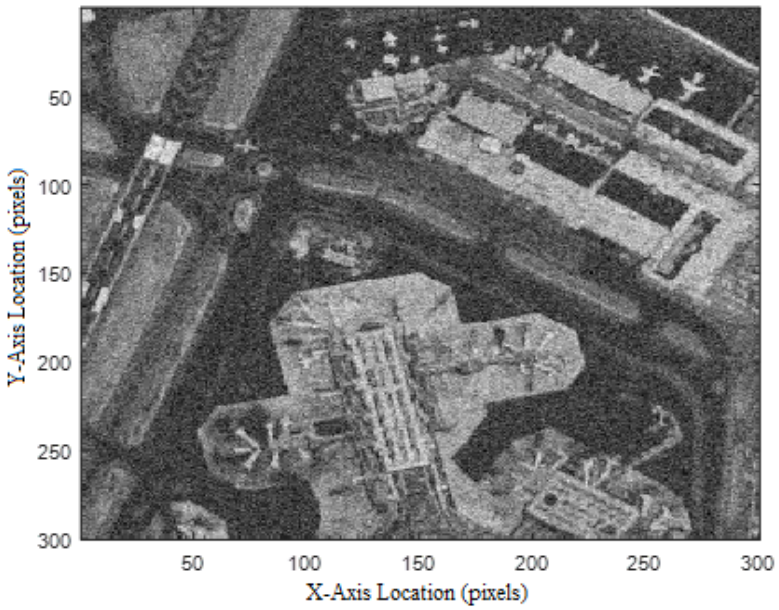

Figure 18. Baseline High Definition Overhead Image with Sensor Noise (Terrestrial)

After applying the modulation transfer function to add jitter blur to the image, objects in the scene became significantly lower in intensity. Additionally, fine features in the baseline high resolution were lost in the blur. As seen in Figure 19, the ability to characterize targets from the sensor's image has decreased due to the vibrations of the reaction wheels. The characterization of the target is critical as it determines the dynamic model for the tracking system. Since the simulation applied an aerial asset's data, the image was brought to a lower resolution to imitate space-based capabilities. The reduced resolution image in Figure 20 became noticeably pixelated and no longer possessed adequate details for identifying targets.

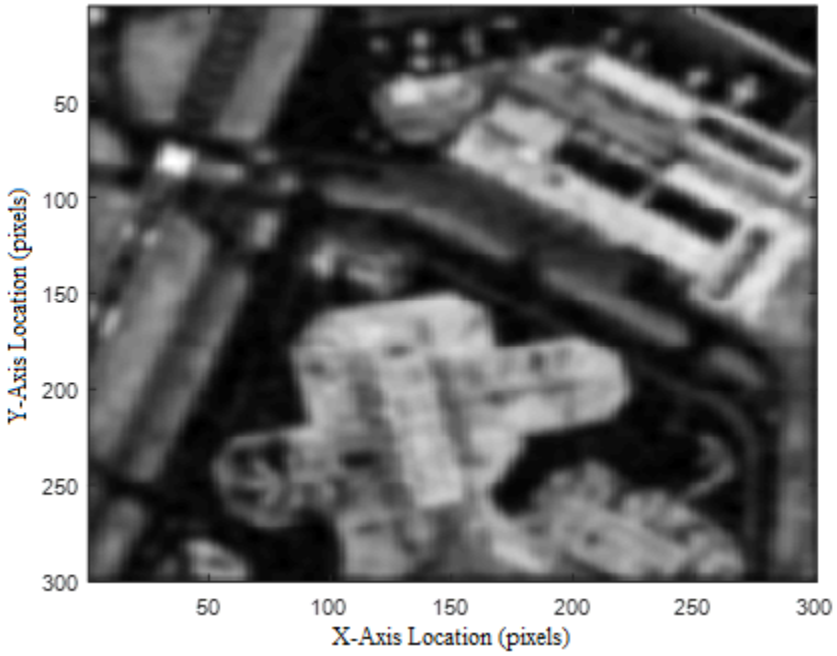

Figure 19. High Definition Overhead Image Subjected to Jitter and Noise (Terrestrial)

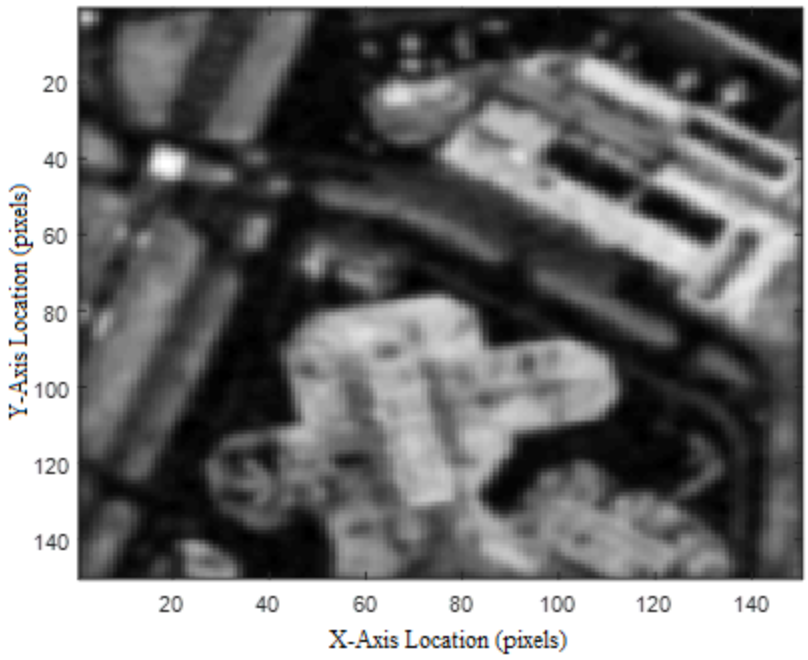

Figure 20. Reduced Resolution Image Subjected to Jitter and Noise (Terrestrial)

C. SIMULATION DETECTION RESULTS

The first simulation frame utilizes Boston Logan International as the baseline high definition image (see Figure 17). The threshold value was set to 1 and was maintained as the default setting with the intent to compare detection performance. In MATLAB, the maximum gray scale intensity value is 255. Therefore, each of the values were divided by 255 to properly scale the image between 0 and 1. The minimal bounding box was set to a value of 3 pixels while the maximum was set to a value of 25 pixels. The bounding box settings were selected to reduce the number of false detections and clutter.

1. Detection at Boston Logan International Airport

In Figure 21, the detection script identified 32 potential targets at the default settings. Picking up multiple aircraft along with structures and areas with high emission, the baseline high definition image possessed the highest probability of detection in comparison to Figures 22 and 23. Figure 22 exhibits the detections in the frame with the jitter blur effects included. Figure 22 provided 9 detections, which is a significant drop in detections. Since the baseline image and the objects in the frame are known, potential

objects-of-interest such as airplanes went undetected and were unable to be characterized in Figure 22. After reducing the resolution of the frame in Figure 23, the amount of detections were further lowered from 9 detections to 7 in which none were objects-of-interest identified from the baseline image.

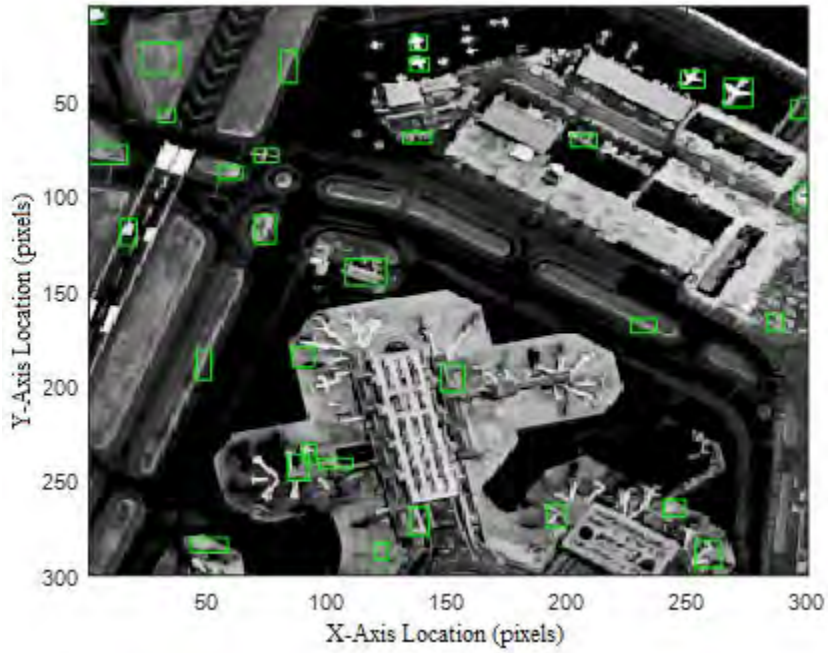

Figure 21. Target Detection on Baseline High Definition Image (Terrestrial)

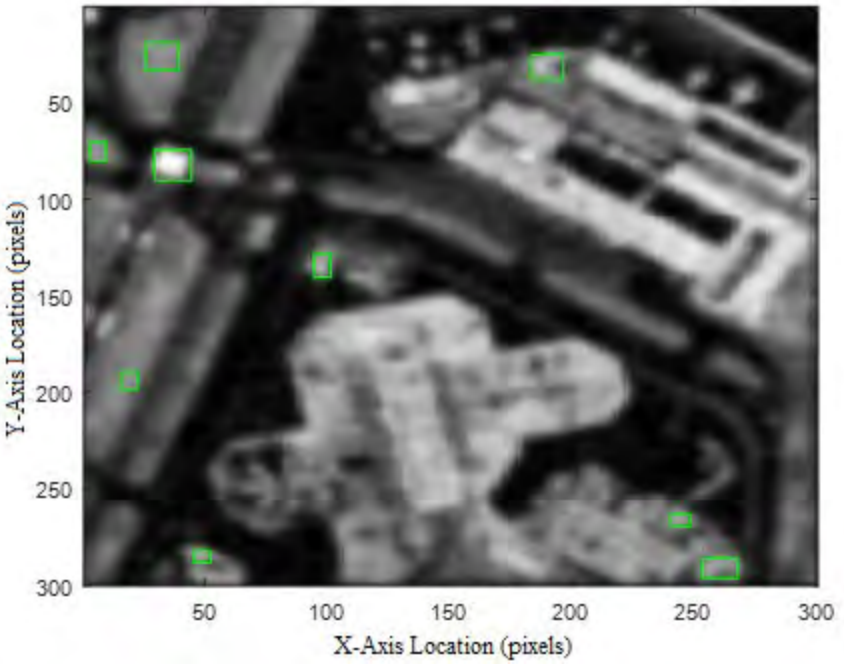

Figure 22. Target Detection on High Definition Image Subjected to Jitter (Terrestrial)

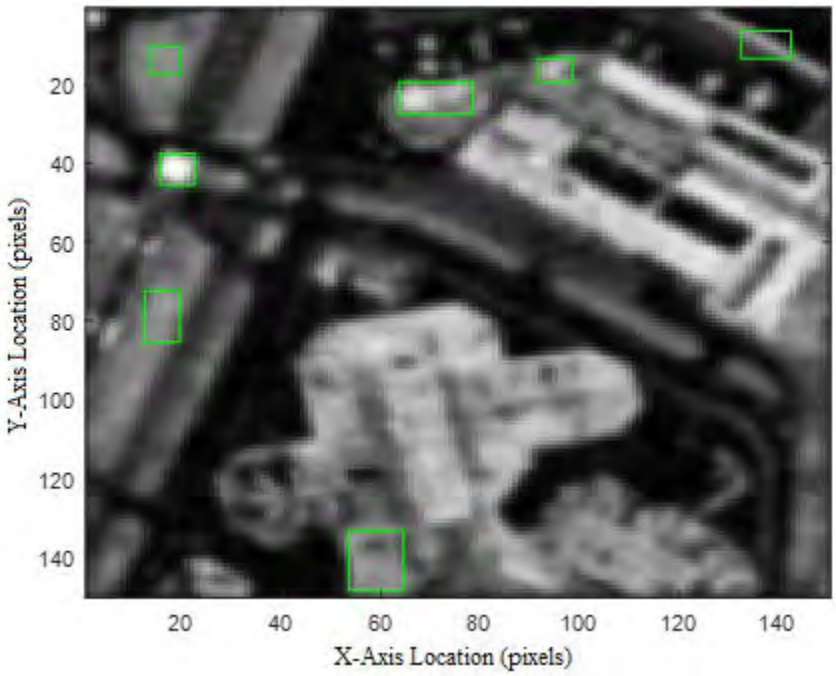

Figure 23. Target Detection on Reduced Resolution Image with Jitter (Terrestrial)

As seen in Figure 24, the average performance for target detection has dropped significantly over a range of detection thresholds. When the simulation implemented jitter blur on the image, the decrease in detections was larger than the reduced resolution image's decrease. This is evidence that the overall intensity of the image has dropped since the exposure time on the targets were shortened.

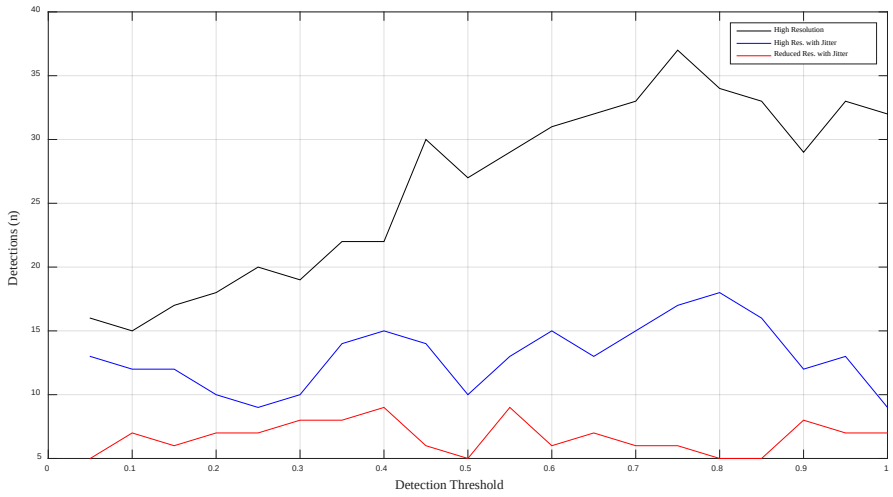

Figure 24. Terrestrial Detection Results—Detection versus Threshold

2. Detection at Harborwalk, Boston

A maritime simulation was also created to see the effects of jitter in a cluttered environment where there were multiple surface vessels in close proximity. In Figure 25, the high resolution image provided distinction between each of the boats in water. When optical blur was applied to the frame, the number of detections dropped, which is consistent with the terrestrial simulation. Additionally, the blur caused an overlapping adjacent targets further reducing the detections and target resolution (see Figure 26). This resulted in multiple boats being treated as a single detection. The effects of jitter blur were further exaggerated in Figure 27 due to the image's reduced resolution.

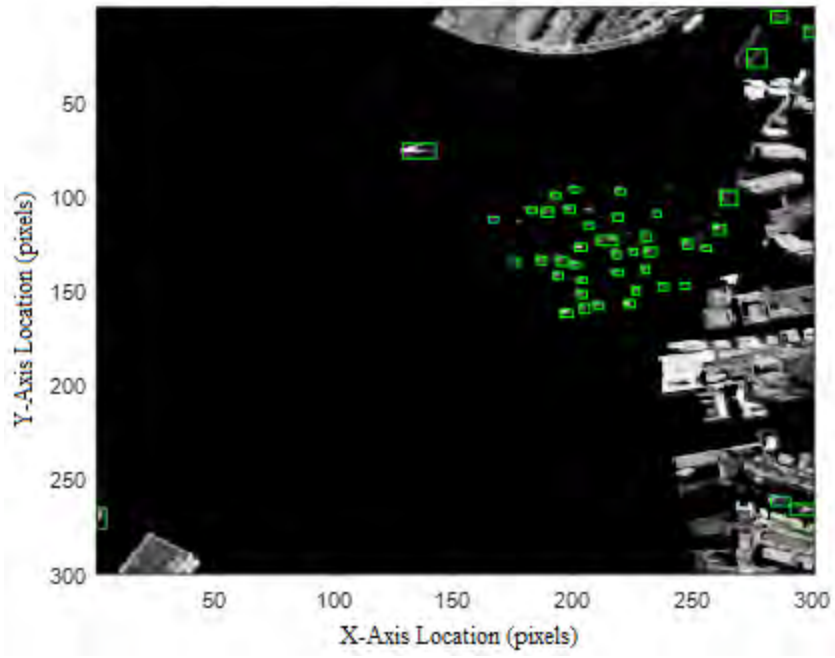

Figure 25. Target Detection on High Definition Overhead Image (Maritime)

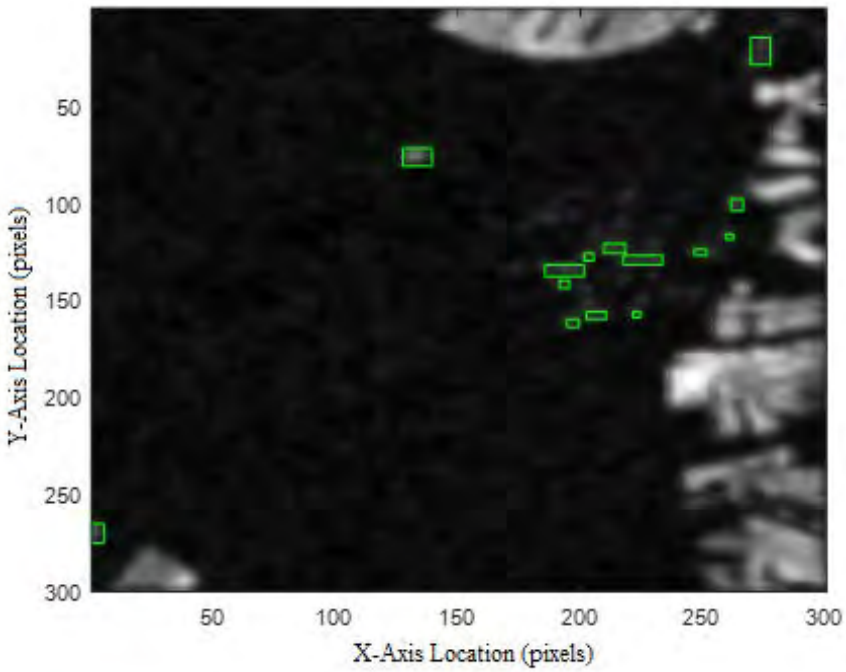

Figure 26. Target Detection on High Definition Overhead Image Subjected to Jitter (Maritime)

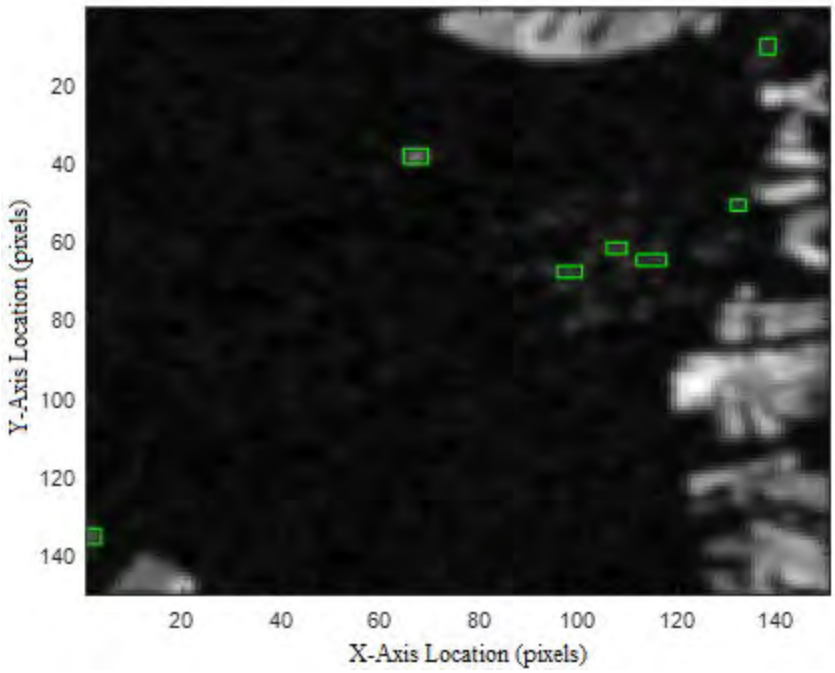

Figure 27. Target Detection on Reduced Resolution Image with Jitter (Terrestrial)

Consistent with the terrestrial simulation, the maritime simulation exhibited the same results when jitter was added and the image's resolution was reduced. Figure 28 exhibits the detections on the three maritime simulations. Since there was a high density of the boats in the maritime image, the simulations performance similarly at 0.5 to 1.0 intensity for the high resolution image with jitter and the reduced resolution image with jitter.

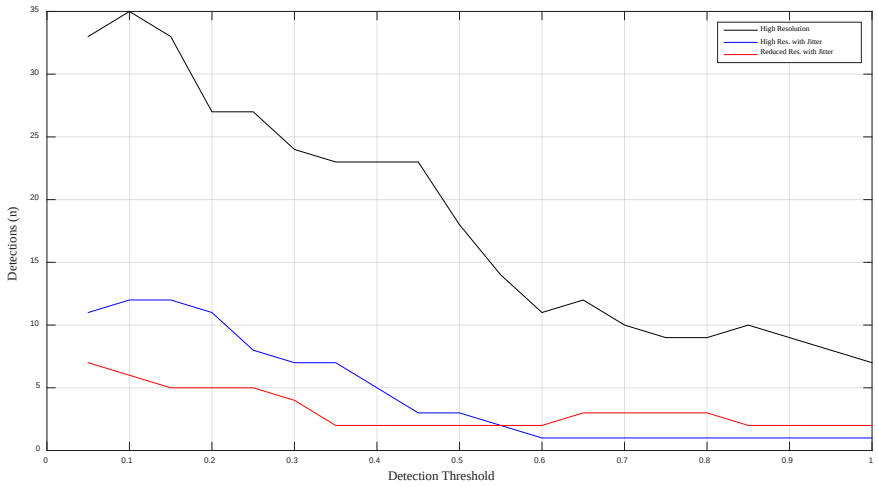

Figure 28. Maritime Detection Results—Detection versus Threshold

D. TRACKING RESULTS

The tracking simulation consisted of an airplane taking off the runway at Boston Logan International Airport. In Figure 29, twenty nine sequential frames were used in the simulation where the asterisks represent target detections and the lines represent the track estimations. During the simulation, the detections and track lines were generated for the moving plane and are shown in Figure 29. When going through the intersection, the plane was lost in the background at the intersection. The airplane generated a new detection and track when it exited the runaway intersection.

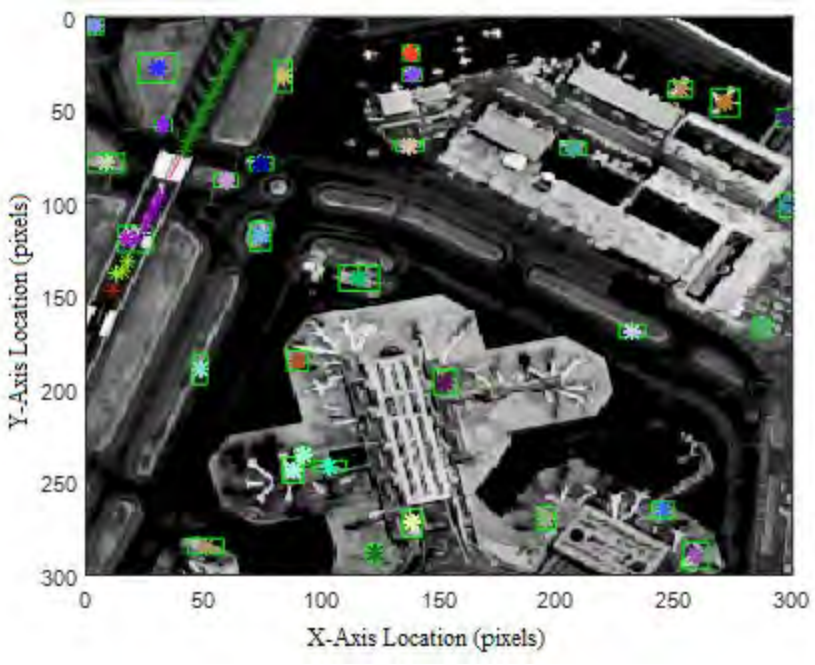

Figure 29. Target Tracking on Baseline High Definition Image

In Figures 30 and 31, the decrease in the number of detections disabled the ability to generate tracks. Although the simulation did provided detections, there weren't enough sequential frames to generate the track lines and provide state estimations for position and velocity. This observation is consistent with the order of the detection-to-engage sequence that is described in Chapter II. Since there were essentially no detections, the sensor measurements that are required by the Kalman filter process were unobtainable. The tracker was furthermore degraded in the reduced resolution images (refer to Figure 23) where only 7 detections were made by the system.

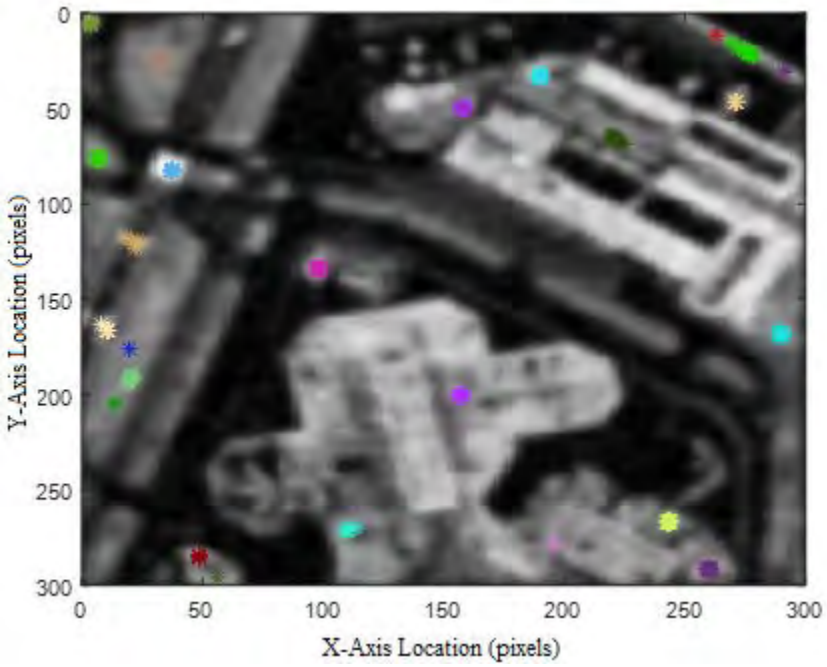

Figure 30. Target Tracking on Baseline High Definition Image with Jitter

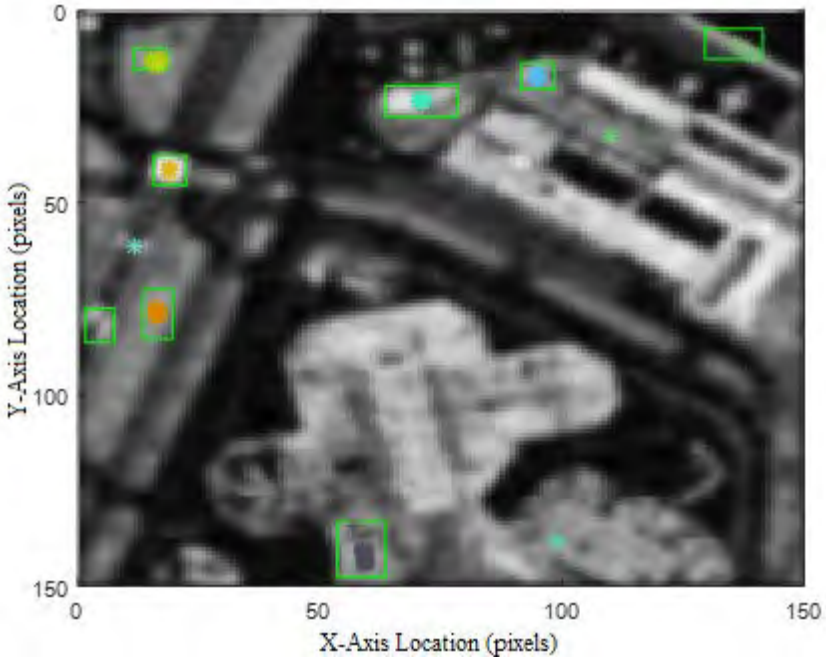

Figure 31. Target Tracking on Reduced Resolution Image with Jitter

In Figure 32, the detection settings were modified by lowering the threshold level by half to compensate for the reduced intensity in the frame. However, even though this change increased the probability of detection in the scene, the amount of false detections were increased. In scenes where the intended target does not possess a high signal-noise-ratio, decreasing the threshold value will also increase the amount of clutter in the background.

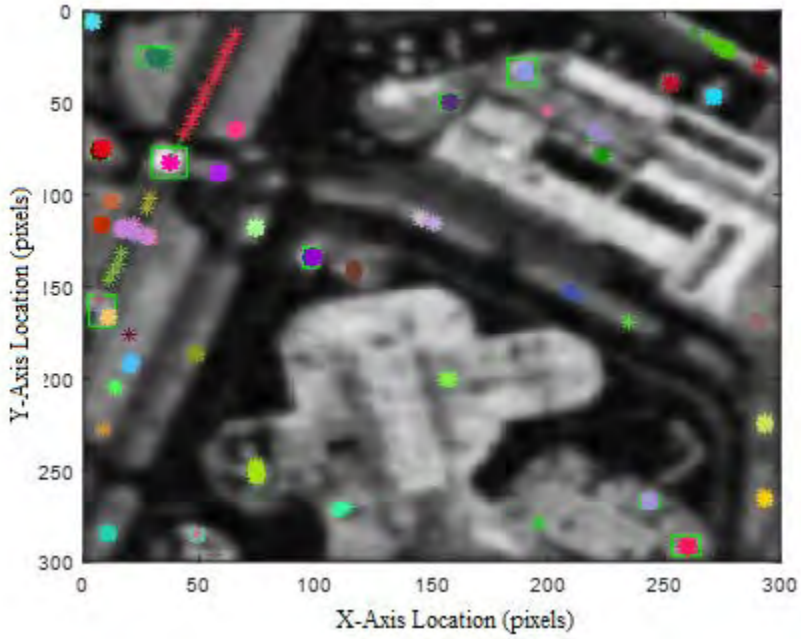

Figure 32. Target Tracking on Baseline High Definition Image with Jitter with Decrease in Threshold Level

Looking at Figures 33 and 34, the estimation performance for the high resolution image with the threshold level of 1 and the jittered imaged with the decreased threshold performed similarly. The similar performance can be attributed to the centroid tracking algorithm, which takes the average position of the detected target.

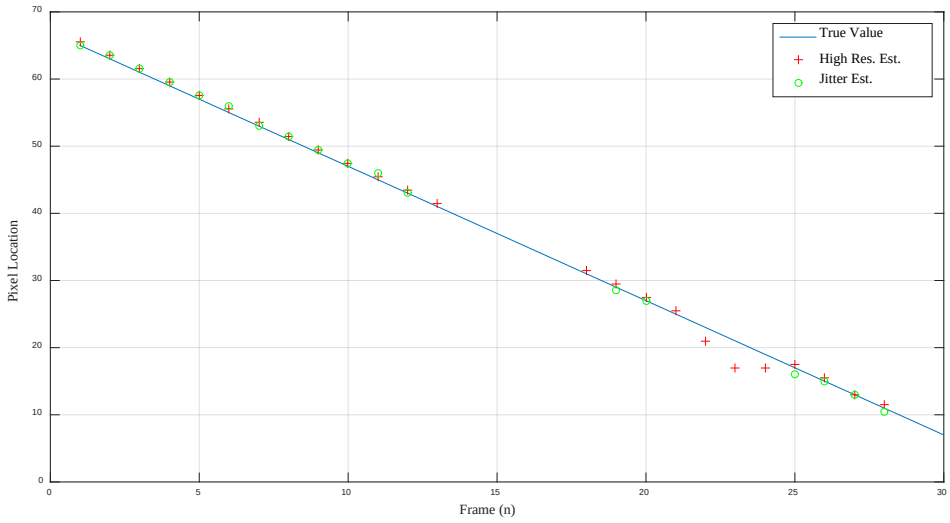

Figure 33. X Position Tracking Results

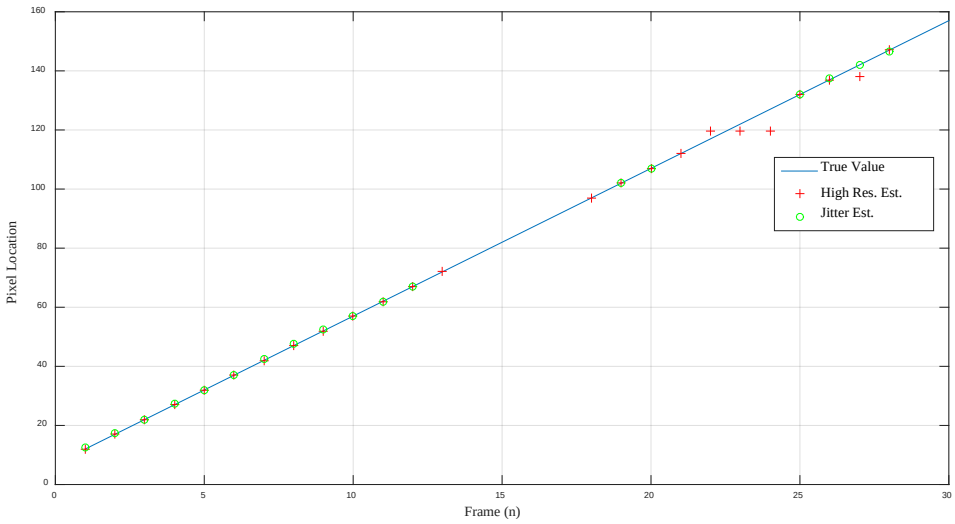

Figure 34. Y Position Tracking Results

THIS PAGE INTENTIONALLY LEFT BLANK

V. INFRARED TRACKING APPLICATIONS FOR HIGH ENERGY LASER BEAM CONTROL RESEARCH TESTBED

The High Energy Laser (HEL) Beam Control Research Testbed (HBCRT) is currently under development as NPS's experimental apparatus for developing beam control technologies. Focusing on the HEL applications, the use of adaptive optics can mitigate refraction and wavefront error due to operating in a turbulent environment. To implement analyze jitter effects on the performance of a system, the HEL is mounted on the Angular Disturbance Simulator (ADS) which simulates ships' and aircrafts' platform motion. Utilizing two infrared sensors for wide-field-of-view and narrow-field-of-view, acquisition, tracking, and pointing (ATP) performance subjected to jitter can be examined.

A. SYSTEM OVERVIEW

The mission sequence for HBCRT's ATP function is analogous to the detect-to-engage sequence described in Chapter II. The initial phase for the HBCRT is target cueing. During target cuing the ATP system conducts state estimation and target discrimination from the background [16]. After the target cueing phase, the HBCRT optimally points toward the target and passively tracks it. Line-of-sight stabilization while tracking will be accomplish through the use of a fast steering mirror. After passively tracking the target, the HBCRT begins actively tracking the target utilizing a continuous wave fiber laser. This will illuminate the target and provide ranging information. While actively tracking the target, the aimpoint is selected for scoring the target with the HEL. The aimpoint is constantly maintained until the track is neutralized [16].

The HBCRT consists of three assemblies that perform the required functions mentioned in the previous paragraph. The three assemblies are the beam director assembly (BDA), beam control assembly (BCA), and angular distance simulator (ADS) [16]. The BDA consists of a 30 centimeter telescope with an inertial reference unit (IRU). Figure 35 is a depiction of the three assemblies put together.

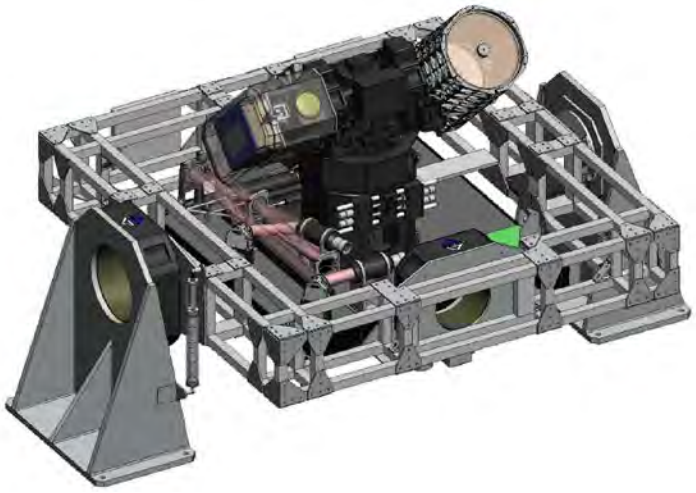

Figure 35. High Energy Laser Beam Control Research Testbed

Source [6]: M. R. Krueger, "A comparison of detection and tracking methods as applied to OPIR optics," M.S. thesis, Dept. Astronautical Eng., Naval Postgraduate School, Monterey, CA, 2014.

The beam control assembly provide the tracking and laser pointing functions for the HBCRT. This assembly is also capable of providing wavefront corrections through sensing and control [16].

B. INFRARED WIDE-FIELD-OF-VIEW

Operating in the $0.9\,\mu m$ to $1.7\ \mu m$ band, the Xenics Bobcat-640-CL camera performs as the wide-field-of-view sensor (see Figure 36) [22]. The Xenics camera provides frames footage of 640 x 512 resolution at the maximum rate of 100 Hz. The integration time range for each frame is between $1\,\mu s$ to 40 ms.

Figure 36. Bobcat-640-CL Camera

Source [22]. Bobcat-640-CL. Xenics Infrared Solutions. [Online] Available: http://www.xenics.com/en/bobcat-640-cl

C. INFRARED NARROW-FIELD-OF-VIEW

The acquisition track sensor (ATS) provides a wide-field of view search and detection capability for the HBCRT. Using a FLIR SC6000 medium wave infrared camera (see Figure 37), the ATS is able to able to capture frames at the resolution of 640 X 512 pixels at the rate of 126 Hz [23].

Figure 37. FLIR SC6000 MWIR Camera

Source [23]. FLIR SC6000 series MWIR science grade camera. FLIR. [Online]. Available:http://www.flirmedia.com/MMC/THG/Brochures/RND_016/RND_016_US.pdf

The FLIR SC6000 MWIR is coupled with a Janos zoom lens which is capable of zooming to 50/250/500 mm [16]. Together, these two systems construct a passive infrared detection system that can identify and track potential targets.

D. ANGULAR DISTURBANCE SIMULATOR

In order to simulate the motion naval platforms, the angular disturbance simulator (ADS) creates base motion in the roll and pitch axis. While the ADS provides the large sweeping angular maneuvers, proof mass actuators provide high frequency (>50 Hz) vibrations to simulate the system's mechanical components operation [16]. Using these two systems, expected platform motion of a sensor or laser platform can be programmed into the ADS. This enables the developments and analysis of real-time control of a fast steering mirror to mitigate the effects of a moving platform.

VI. CONCLUSIONS

The final chapter encompasses and bridges the results of this thesis and future avenues of research related to jitter and OPIR missions. The first section summarizes the simulation results as they apply to detection, characterization, and tracking performance. The second section provides possible areas for future research and testing.

A. SUMMARY

The jitter generated by the static and dynamic imbalances of the reaction wheels degraded the detection and tracking performance in the terrestrial and maritime simulations. The magnitude and frequency of the jitter directly correlated with the angular velocity of the reaction wheels. As the angular velocity and magnitude of the reaction wheels increased, so did the amount of optical jitter blur on the sensor's image.

The jitter blur on the image frame resulted in a decrease of the target-of-interest's intensity. The reduction in intensity, when significant enough, caused the target to fall below the detection threshold. As seen from the simulations, objects of interest, such as planes and ships, went undetected in an environment subjected to high amounts of jitter. Additionally, the jitter made the unique identifiers of the intended targets unrecognizable. In regard to tracking performance, the reduced the number of detections degraded the targets' track association within a series of frames.

The results of this thesis stressed the importance of system-level design for remote sensing. Mission performance relies not only on the capabilities of the sensor and payload but also heavily on the subsystems of the spacecraft's bus.

B. FUTURE WORK

In Professor Brij Agrawal's paper, "Jitter Control for Imaging Spacecraft," reaction wheels are not the only source of jitter on a spacecraft [24]. Cryogenics for infrared payloads also cause unwanted vibrations on a spacecraft. Thermal shocks from the spacecraft entering or exiting a period of eclipse cause additional vibrations on the spacecraft's structure. Both solar drive-motors, which orient the spacecraft's solar arrays

toward the sun's radiation, and thrusters, which control attitude control and desaturate momentum, contribute vibrations to the spacecraft. Future work should consider adding the vibration and torque sources that Professor Agrawal mentioned in his paper to construct a more comprehensive model for operations.

The model used in the simulations assumed a rigid body for the variations in the spacecraft's attitude. Future work can encompass a flexible spacecraft model that will include multiple vibrational modes. Since the reaction wheels in the attitude control system operate at a range of speeds, vibrational analysis with a dynamic model should be investigated.

The implementation of image processing techniques from Michael Krueger's thesis can be integrated into the jitter-subjected frames. Image processing techniques, such as the local contrast method (LCM) or principle component analysis (PCA), can increase the signal-to-noise ratio of the target to the background. Utilizing these processing techniques could increase target detection and lower the reaction wheel imbalance requirements for the attitude control system.

Finally, since the findings in this thesis were enabled though MATLAB simulations, future works should incorporate the implementation and validation of the effect of jitter with the use of hardware. Once the High Energy Laser Beam Control Research Testbed (HBCRT) is constructed and delivered, the simulated reaction wheel jitter can be programed into the angular disturbance simulator (ADS). While the ADS is operating, the wide-field-of-view infrared sensor can be utilized for detection and tracking in order to validate what was accomplished in the results.

APPENDIX. MATLAB CODE

```
% Initialization File for Simulink File
% ////////////////////////////////////////////////////////////////
clc, clear all, format compact

% ++++++++++++++++++++
% GIVENS AND CONSTANTS
% ++++++++++++++++++++

mu = 3.98601*10^5;      % km^3/s^2      Mu of Earth
r  = 26800;             % km            Radius of orbit

w0 = sqrt(mu/r^3);      % 1/s           Orbital frequency

M = 1763;               % kg            Mass of spacecraft

Jx = XXX;               % kg-m^2        X axis inertia
Jy = XXX;               % kg-m^2        Y axis inertia
Jz = XXX;               % kg-m^2        Z axis inertia


J = diag([Jx Jy Jz]);

% +++++++++++++++++++++++++
% DEFINE INITIAL CONDITIONS
% +++++++++++++++++++++++++

x0(1) =   0;            % deg           Initial roll (X) angle
x0(2) =   0;            % deg           Initial pitch (Y) angle
x0(3) =   0;            % deg           Initial yaw (Z) angle
x0(4) = 0.0;            % deg/s         Initial roll (X) rate
x0(5) = 0.0;            % deg/s         Initial pitch (Y) rate
x0(6) = 0.0;            % deg/s         Initial yaw (Z) rate

x0 = x0*pi/180;         % Initial state vector (rad and rad/s)

q0(1) = sin(x0(1)/2)*cos(x0(2)/2)*cos(x0(3)/2)-
cos(x0(1)/2)*sin(x0(2)/2)*sin(x0(3)/2);
q0(2) =
cos(x0(1)/2)*sin(x0(2)/2)*cos(x0(3)/2)+sin(x0(1)/2)*cos(x0(2)/2)*sin(x0
(3)/2);
q0(3) = cos(x0(1)/2)*cos(x0(2)/2)*sin(x0(3)/2)-
sin(x0(1)/2)*sin(x0(2)/2)*cos(x0(3)/2);
q0(4) =
cos(x0(1)/2)*cos(x0(2)/2)*cos(x0(3)/2)+sin(x0(1)/2)*sin(x0(2)/2)*sin(x0
(3)/2);

xDes(1) = 0;
xDes(2) = 0;
xDes(3) = 0;
```

```
xDes(4) = 0;
xDes(5) = 0;
xDes(6) = 0;

% +++++++++++++++
% DEFINE Z MATRIX
% +++++++++++++++

b1 =      0;                % RW1 rotation about Y axis
b2 =      0;                % RW2 rotation about Y axis
b3 =    270;                % RW3 rotation about Y axis
b4 = -35.27;                % RW4 rotation about Y axis

th1 =  0;                   % RW1 rotation about Z axis
th2 = 90;                   % RW2 rotation about Z axis
th3 =  0;                   % RW3 rotation about Z axis
th4 = 45;                   % RW4 rotation about Z axis

UVX = [1;0;0];              % Unit vector pointing along negative X
axis

% Perform C2 rotation by beta then C3 rotation by theta

RW1h = C3(th1)*C2(b1)*UVX;  % RW1 unit momentum vector
RW2h = C3(th2)*C2(b2)*UVX;  % RW2 unit momentum vector
RW3h = C3(th3)*C2(b3)*UVX;  % RW3 unit momentum vector
RW4h = C3(th4)*C2(b4)*UVX;  % RW4 unit momentum vector

Z = [RW1h RW2h RW3h RW4h]   % Z matrix

pinvZ = pinv(Z);            % Pseudoinverse of Z matrix

% +++++++++++++++++++++++++++++++++
% DEFINE REACTION WHEEL PERFORMANCE
% +++++++++++++++++++++++++++++++++

hDotMax = 0.1;              % Nm        Maximum torque (hDot)
hMax    = 20;               % Nms       Maximum angular momentum
rpmMax  = 2500;             % rpm       Maximum rotational rate
wMax    = rpmMax*2*pi/60;   % rad/sec   Maximum angular velocity
JRW     = hMax/wMax;        % kg-m^2    Reaction wheel moment of
inertia

% +++++++++++++++++++++++++++++++++++++++
% DEFINE EULER AXIS AND DESIRED QUATERNION
% +++++++++++++++++++++++++++++++++++++++

e = Z(:,4);                 % Euler axis

a = 120;                    % Euler rotation angle (degrees)
a = 0;

%qC(1) = e(1)*sind(a/2);     % q1 desired (commanded)
```

```
%qC(2) = e(2)*sind(a/2);     % q2 desired (commanded)
%%qC(3) = e(3)*sind(a/2);     % q3 desired (commanded)
qC(1) = 0;     % q1 desired (commanded)
qC(2) = 0;     % q2 desired (commanded)
qC(3) = 0;     % q3 desired (commanded)
qC(4) = cosd(a/2);          % q4 desired (commanded)

q1c = qC(1);
q2c = qC(2);
q3c = qC(3);
q4c = qC(4);

Q = [ q4c  q3c -q2c -q1c;
     -q3c  q4c  q1c -q2c;
      q2c -q1c  q4c -q3c;
      q1c  q2c  q3c  q4c];

% ++++++++++++++++++++
% DEFINE GAINS K AND C
% ++++++++++++++++++++

%K = 0.5;
%C = 5.0;

%This is 10^-4
K = 150;
C =160;


%Create RW Disturbance Torque
%/////////////////////////////////////////////////////////////////////////
function [Dynamic_Torque,Static_Torque]= fcn(w,t)
%#codegen

%Wheel Static Imbalance
Sx=5*10^-6;                 %(kg*m^2)
Sy=5*10^-6;                 %(kg*m^2)
Sz=5*10^-6;                 %(kg*m^2)
S4=5*10^-6;                 %(kg*m^2)


%Distance Between Reaction Wheel and CM
R=[0.35; 0.35; 0.35];

phix=0;
phiy=0;
phiz=0;
phi4=0;

%Static Torque
%Static Disturbance Force From 3 Reaction Wheels
F=[(Sy*w(2)^2*cos(w(2)*t*phiy))+(Sz*w(3)^2*cos(w(3)*t*phiz));
   (Sz*w(3)^2*cos(w(3)*t*phiz))+(Sx*w(1)^2*cos(w(1)*t*phix));
```

```
   (Sx*w(1)^2*cos(w(1)*t*phix))+(Sy*w(2)^2*cos(w(2)*t*phiy))];

%Adding the Force of the 4th Reaction Wheel
A=[1 0 0;
    0 cosd(45) sind(45);
    0 -sind(45) cosd(45)];

B=[cosd(-45) sind(-45) 0;
    -sind(-45) cosd(-45) 0;
    0 0 1];

C=A*B;

F4=inv(C)*[S4*w(4)^2*cos(w(4)*t+phi4);
           S4*w(4)^2*sin(w(4)*t+phi4);
           0];
%Summation of Force of all Reaction Wheels
%F=F+F4;

%Computation of Torque
Static_Torque=cross(R,F)+cross([0.35 ;0.35 ;0.35],F4);

%Dynamic Torque
%Wheel Dynamic Imbalance
Dx=1*10^-6;                 %(kg*m^2)
Dy=1*10^-6;                 %(kg*m^2)
Dz=1*10^-6;                 %(kg*m^2)
D4=1*10^-6;                 %(kg*m^2)

phix1=0;
phiy1=0;
phiz1=0;
phi41=0;

Dynamic_Torque=[(Dz*w(3)^2*sin(w(3)*t+phiz1))-
(Dy*w(2)^2*sin(w(2)*t+phiy1));
                (Dx*w(1)^2*sin(w(1)*t+phix1))-
(Dz*w(3)^2*sin(w(3)*t+phiz1));
                (Dy*w(2)^2*sin(w(2)*t+phiy1))-
(Dx*w(1)^2*sin(w(1)*t+phix1))];
%////////////////////////////////////////////////////////////////////
function hDot = fcn(q,wBN,wBO,h,J,Z,Q,K,C)

% Calculate Quaternion Error

q1 = q(1);
q2 = q(2);
q3 = q(3);
q4 = q(4);

q = [q1 q2 q3 q4]';

qe = Q*q;
```

```
qe = qe(1:3);

% Calculate Required Torque in Body Frame

Treq = -K.*J*qe-C.*J*wBO+cross(wBN,(J*wBN));

% Calculate Required Torque in Reaction Wheel Frame

hDot = pinv(Z)*(-Treq-cross(wBN,(Z*h)));
%//////////////////////////////////////////////////////////////////
function Tout = fcn(wBN,h,hDot,Z)

% Calculate Actual Torque Produced by Reaction Wheels

Tout = -(cross(wBN,(Z*h))+Z*hDot);
%//////////////////////////////////////////////////////////////////
```

THIS PAGE INTENTIONALLY LEFT BLANK

LIST OF REFERENCES

[1] R. M. Gates and J. R. Clapper. (2011). National security space strategy unclassified summary. [Online]. Available: https://fas.org/irp/eprint/nsss.pdf

[2] C. Chaplain, "Space acquisitions: Assessment of overhead persistent infrared technology report," U.S. Government Accountability Office, Washington, DC, GAO-14-287R, 13 January. 2014.

[3] NASA works to control spacecraft motions. (1993, July). NASA. [Online]. Available: http://www.nasa.gov/centers/langley/news/factsheets/Spacecraft.html.

[4] K. Liu, P. Maghami and C. Blaurock, "Reaction wheel disturbance modeling, jitter analysis, and validation tests for Solar Dynamics Observatory," presented at AIAA Guidance, Navigation and Control Conference Exhibit, Honolulu, HI, 2008.

[5] L. Liu, "Jitter and basic requirements of the reaction wheel assembly in the attitude control system," Massachusetts Institute of Technology, Cambridge, MA, 2007.

[6] M. R. Krueger, "A comparison of detection and tracking methods as applied to OPIR optics," M.S. thesis, Dept. Astronautical Eng., Naval Postgraduate School, Monterey, CA, 2014.

[7] (2015, Jun 5). *Remote Sensing Systems Directorate*. Available: http://www.losangeles.af.mil/library/factsheets/factsheet.asp?id=5514.

[8] (2013, April 19). *Scalable Neuroscience and the Brain Activity Mapping Project.* Available: http://cs.brown.edu/people/tld/note/blog/13/04/19/.

[9] K. Kasunic, *Optical systems engineering.* New York, NY: The McGraw-Hill Companies, 2011.

[10] C. Payne, *Principles of Naval Weapon Systems.* Annapolis, MD: United States Naval Institute, 2010.

[11] B. Allen. Atmospheric aerosols: what are they, and why are they so Important?. (2015, Jul). NASA. [Online]. Available: http://www.nasa.gov/centers/langley/news/factsheets/Aerosols.html.

[12] H. Hogan. With infrared, military owns more than the night. (2013, Apr) Photonics Spectra. [Online]. Available: http://www.photonics.com/Article.aspx?AID=53438.

[13] MK46 MOD1 optical sight system. (2008, April 7). L3 Communications Holdings. [Online]. Available: http://www2.l-3com.com/keo/pdfs/AD39%20MK46%20MOD%201%20datasht.pdf.

[14] Advanced targeting forward looking infrared [ATFLIR]. Raytheon. [Online]. Available: http://www.raytheon.com/capabilities/products/atflir/.

[15] Small satellite reaction wheels. Clyde Space. [Online]. Available: http://www.clyde-space.com/products/reaction_wheels.

[16] J. Kim, *private communication*, Sep. 2015.

[17] "Satellite Attitude Control System Design Using Reaction Wheels," Aerospace Power & Electronics Simulation Workshop. [Online]. Available: academics.auohio.edu/simond/pubs/Gouda04.pdfcademic.cs.

[18] "NPS-AE3818 Unit 2, Introduction to State Space Control," class notes for Spacecraft Attitude, Determination, and Control, Dept. of Mechanical and Aerospace Engineering, Naval Postgraduate School, Monterey, CA, fall 2015.

[19] P. Merrit, *Beam Control for Laser Systems.* Albuquerque: The Directed Energy Professional Society, 2012.

[20] Y. Bar-Shalom, L. Xi and T. Kirubarajan, *Estimation with Applications To Tracking and Navigation*, New York: John Wiley & Sons, Inc, 2001.

[21] U.S. Geological Survey Earth Resources Observation and Sciences. NP0NAPP0019999.TIF [Online] Available: http://glovis.usgs.gov/. Accessed Sep, 30, 2015.

[22] Bobcat-640-CL. Xenics Infrared Solutions. [Online] Available: http://www.xenics.com/en/bobcat-640-cl

[23] FLIR SC6000 series MWIR science grade camera. FLIR. [Online]. Available: http://www.flirmedia.com/MMC/THG/Brochures/RND_016/RND_016_US.pdf

[24 B. Agrawal. Jitter control for imaging spacecraft. IEEE. [Online]. Available: http://ieeexplore.ieee.org/stamp/stamp.jsp?arnumber=5158266

INITIAL DISTRIBUTION LIST

1. Defense Technical Information Center
   Ft. Belvoir, Virginia

2. Dudley Knox Library
   Naval Postgraduate School
   Monterey, California